Emerging Exciton Physics in Transition Metal Dichalcogenide Heterostructures

Emma C. Regan[1,2,3], Danqing Wang[1,2,3], Eunice Y. Paik[4], Yongxin Zeng[5], Long Zhang[4], Jihang Zhu[5], Allan H. MacDonald[5*], Hui Deng[4*], Feng Wang[1,3,6*]

[1] Department of Physics, University of California at Berkeley, Berkeley, California 94720, United States

[2] Graduate Group in Applied Science and Technology, University of California at Berkeley, Berkeley, California 94720, United States

[3] Material Science Division, Lawrence Berkeley National Laboratory, Berkeley, California 94720, United States

[4] Department of Physics, University of Michigan, Ann Arbor, MI, USA

[5] Department of Physics, University of Texas at Austin, Austin, TX 78712, USA

[6] Kavli Energy NanoSciences Institute at University of California Berkeley and Lawrence Berkeley National Laboratory, Berkeley, California 94720, United States

* Correspondence to: macd@physics.utexas.edu, dengh@umich.edu, fengwang76@berkeley.edu

Abstract:

Atomically thin transition metal dichalcogenides (TMDs) are two dimensional semiconductors with tightly bound excitons and correspondingly strong light matter interactions. Due to weak van der Waals bonding between layers, TMDs can be isolated and stacked together to form synthetic heterostructures with emergent electronic and excitonic properties. In this review, we focus on the emergent exciton physics in moiré superlattices and in TMD heterostructures coupled to optical cavities, where exciton behavior can be dramatically modified by the environment. In moiré superlattices, a small twist angle or lattice mismatch between layers introduces a periodic variation in the interlayer alignment that leads to exciton localization, modified optical selection rules, and strong correlations. In cavity-heterostructure systems, light-matter interaction is enhanced, and exciton states can couple to the cavity to form exciton-polaritons whose properties depend on the specific TMD layers involved and their alignment. Here, we discuss recent theoretical and experimental progress towards realizing exotic exciton states in TMD heterostructures and comment on future scientific and technological directions.

Main Text

Introduction:

Atomically thin transition metal dichalcogenides (TMDs) are a diverse family of materials with rich electronic and optical properties. In their bulk form, TMDs are layered materials with weak interlayer van der Waals interactions. Consequently, TMDs can be mechanically and chemically isolated into few-layer and single-layer (monolayer) crystals. Many monolayer TMDs – including the intensely-studied set of MoS_2, $MoSe_2$, WS_2, and WSe_2 – are semiconductors with direct bandgaps at visible and near-infrared energies. In these materials, electrons and holes form tightly-bound excitons due to their attractive Coulomb interaction and the reduced screening in the two dimensional (2D) environment. The excitons dominate the optical properties of monolayer TMDs, absorbing a large fraction of incident light at the exciton resonance and inspiring interest in optoelectronic device applications.

Stacks of TMDs, along with other 2D materials such as few-layer graphite (flG) and hexagonal boron nitride (hBN), provide a platform for highly tunable, synthetic quantum materials[1]. Unlike three dimensional heterostructures that are limited by epitaxial growth, 2D heterostructures have enormous flexibility: since the layers are held together with weak van der Waals bonds, the constituent layers can have arbitrary lattice mismatch and relative twist angle. Polymer-based transfer techniques are used to carefully control the stacking process[2–4], providing a method for creating physical systems with precise geometries and diverse emergent properties. 2D heterostructures can be further controlled via electrostatic gating, in which metallic gates (flG or choice bulk metals) and dielectrics (typically hBN or SiO_2) can be integrated to tune the electric field and carrier concentration of the heterostructure in situ. Here we define heterostructure broadly to include both stacks of the same materials and stacks containing different materials.

TMD heterostructures have become a fruitful material platform for realizing emergent excitonic states, including states in which correlations and topology play a major role. In addition to exciton states localized in each TMD monolayer, the heterostructure may also support new emergent exciton states. Interlayer excitons, in which electrons and holes reside in different layers[5,6], are an important example. Interlayer excitons can be the lowest energy excitons in a heterostructure, due to band alignment or an applied electric field, and therefore are prominent in emission measurements. In this review, we focus on two methods for manipulating exciton states in 2D heterostructures that have particularly dramatic and fascinating effects: the introduction of a moiré superlattice and formation of an optical cavity.

A moiré superlattice offers a powerful method to engineer excitonic states in TMDs. A twist angle or lattice mismatch between two monolayers introduces a periodic variation in the interlayer alignment across the heterostructure. This variation produces a periodic potential energy landscape for electrons and holes, and therefore also excitons. When the moiré potential is large, the moiré superlattice dramatically affects both intralayer and interlayer excitons, resulting in exciton localization[7–10], modified optical selection rules[7,11,12], and even emergent interactions with correlated electronic states[13–15].

Optical cavities provide another interesting way to control excitonic behavior through enhanced light-matter interaction. In the strong coupling limit, excitonic modes couple to optical cavity modes and form exciton-polariton states. Here, excitons in cavities retain certain properties of the excitons, such as their valley selection rules and coherence, but also show fascinating emergent properties[16–18].

In this review, we begin with an introduction to excitons in monolayer TMDs. We then discuss theoretical proposals for and experimental demonstrations of emergent exciton behavior

in moiré superlattices and in optical cavities. Finally, we comment on scientific goals that may soon be realized with TMD heterostructures, such as realizing high-temperature exciton condensation and moiré exciton-polaritons.

Excitons in TMD heterostructures

Excitons in TMD monolayers

Understanding excitons in TMD heterostructures starts with understanding the electronic and excitonic states in TMD monolayers. Here we focus on the 2H phase MX_2 compounds (Fig. 1a) with M = (Mo, W) and X = (S, Se), which are stable under ambient conditions and have been the emphasis of much recent work in both monolayers and heterostructures[19,20]. As the TMDs are thinned to the monolayer limit, the bandgap transitions from indirect to direct, with the band extrema at the K and K' corners of the hexagonal Brillouin zone[21,22] (Fig. 1b). Monolayer TMDs have broken inversion symmetry, so spin-orbit coupling is strong and the K and K' valleys exhibit valley-contrasting Berry curvature and orbital magnetic moments[23,24].

In a 2D environment, dielectric screening of the Coulomb interactions between electrons and holes is reduced, leading to tightly-bound exciton states at the K and K' valleys[25,26] (Fig. 1b). The exciton binding energies can be hundreds of millielectronvolts, an order of magnitude larger than in typical bulk semiconductors like GaAs[27,28]. The corresponding exciton Bohr radius is a few nanometers and extends over several lattice periods. Due to their large binding energies, excitons can have large oscillator strengths and dominate the optical properties of monolayer TMDs at cryogenic and room temperatures[18]. Further, excitation with σ^+ and σ^- circularly polarized light creates K and K' excitons, respectively, providing convenient access to the valley degree of freedom[29–34].

The conduction and valence bands at K and K' are largely composed of transition metal *d* orbitals, allowing spin-orbit coupling to be strong, unlike in graphene[35–37]. At the valence band maximum, the spin splitting is large: around 0.2 eV for Mo-based TMDs[21,22] and 0.4 eV for W-based TMDs[38,39]. A smaller spin splitting occurs in the conduction band, which has different sign depending on the metal atom[40,41]. Consequently, the lowest energy exciton is optically bright (electron and hole of same spin) in Mo-based TMDs and dark (opposite spin) in W-based TMDs[42]. This detail has important consequences for light emission since the lower-energy dark state in W-based materials dramatically reduces emission at low temperatures[43]. Additionally, the spin splitting has opposite signs in the K and K' valleys because of time reversal symmetry, which effectively locks the spin and valley degrees of freedom: the bright exciton is spin up in one valley and spin down in the other[36]. Therefore, the valley optical selection rule also gives direct access to spin in monolayer TMDs.

Excitons in TMD heterostructures

Several factors are important in determining the properties of excitons in a TMD heterostructure: the electronic structure of each monolayer, the relative band alignment between layers, and the twist angle (θ) and lattice mismatch between the layers (δ) (Fig. 1c). In TMDs, interlayer coupling at the K and K' points is relatively weak, so it is commonly assumed that the monolayer electronic states are largely localized within individual layers[44,45]. This assumption is particularly reasonable in heterostructures with large twist angles or lattice mismatches since the Brillouin zones of each layer are shifted, suppressing interlayer coupling. When the twist angle is small and the bands are close in energy, interlayer hybridization can occur, as one might expect considering the change from direct to indirect bandgaps in bilayer TMDs. Recently, it has been

shown that the twist angle and lattice mismatch between layers in a heterostructure strongly impact its physical properties, as we discuss in detail in the "moiré superlattice" section.

Bilayers formed from two of the common semiconducting TMDs – MoS_2, $MoSe_2$, WS_2, and WSe_2 – are type II heterostructures, where the lowest conduction band and highest valence band are in different materials[46,47] (Fig. 1d). In this case, the excitons at the K and K' valleys within each layer (intralayer excitons) are similar to their monolayer counterparts but with additional screening from the neighboring material[48,49]. Lower-energy interlayer exciton states, where the electron and hole reside in different layers[5,6], also exist. The spatial separation of the electron and hole gives interlayer excitons fascinating properties: they have long valley lifetimes due to reduced exchange interactions[10,50], their energies can be tuned with electric fields because of their permanent electric dipole moment[6], and they show promise for Bose-Einstein condensation[51,52].

Interlayer excitons can be optically bright or dark depending on the stacking configuration of the layers[53–55]. Although the oscillator strength of interlayer excitons is relatively small due to the spatial separation between electrons and holes, interlayer excitons can dominate the emission of heterostructures because they are the lowest energy states. In heterostructures with small twist angle (close to 0 degrees or 60 degrees) and small lattice mismatch, the Brillouin zones of the monolayers are nearly aligned, so electrons and holes can recombine and emit photons efficiently. When the conduction band and valence band are misaligned in k-space, the heterostructure has poor emission characteristics: intralayer exciton emission is quenched because the excitons separate faster than their radiative recombination time[6], and the interlayer excitons do not recombine radiatively. Recently, bright interlayer excitons have gained attention for their potential optoelectronic applications.

Interlayer excitons can be formed by optical and electrical methods and are often created by first exciting intralayer excitons. In type II heterostructures, optically excited intralayer excitons quickly separate into electrons in one layer and holes in the other via an ultrafast charge transfer process. Hong *et al.* optically excited MoS_2 intralayer excitons in a MoS_2/WS_2 heterostructure and showed that the hole transfers from the MoS_2 layer to the WS_2 layer within 50 fs[56]. The Coulomb interaction between the spatially separated electrons and holes can then lead to the formation of bound interlayer excitons[57]. It is also possible to directly create interlayer exciton states via resonant optical excitation in aligned heterostructures, but the efficiency is low due to the small absorption of interlayer excitons[12]. Additionally, interlayer excitons can be formed via electrical injection of electrons and holes into the constituent layers[58,59].

Heterostructures formed from two layers of the same material, often called homobilayers, can also support interesting exciton states. Homobilayers can be naturally found bilayer TMDs or artificially stacked TMD monolayers. Due to interlayer hybridization, the lowest energy exciton state becomes momentum indirect, where the gap size depends on the twist angle between the layers[60,61]. Interestingly, electron and hole states at the K and K' valleys remain largely localized within each layer, manifested as the co-existence of both intralayer and interlayer exciton states at the K and K' points in homobilayers[62–64]. Without the type II band alignment, homobilayers have degenerate exciton states in both layers. With an applied electric field, electrons and holes preferentially occupy different layers, and the interlayer exciton dipole orientation is determined by the direction of the applied field[65].

The flexibility in designing a 2D heterostructure – with the materials and twist angle chosen at will – provides several routes to engineer emergent excitonic behavior. In the following sections,

we focus on two particularly powerful tools for tuning intralayer and interlayer excitons in heterostructures: moiré superlattices (Fig. 1e) and optical cavities (Fig. 1f).

Excitons in TMD moiré superlattices

TMD moiré superlattices

The superposition of two atomic lattices in a heterostructure can produce a larger-scale periodicity, called a moiré pattern, which arises from a small difference in the lattice constants of the materials (δ) or a twist angle between their lattices (θ) (Fig. 2a). When δ << 1 and θ << 1, the superlattice periodicity l varies continuously with twist angle as $l = a_0/\sqrt{\delta^2 + \theta^2}$, where $\delta = |a_0' - a_0|/a_0$, and a_0, a_0' are the lattice constants of the two layers. The superlattice periodicity introduces a new length and energy scale that can dramatically modify the electronic and excitonic behavior of the system. On the atomic scale, the alignment between the atoms in each layer varies across the moiré unit cell, creating a periodic potential for electrons and excitons that can be as large as hundreds of millielectronvolts[7,11,66–72]. The potential minima and maxima are usually centered at one of the high symmetry positions in the lattice, labelled A, B, and C in Fig. 2a. Hybridization of the electronic states in the two layers can further modify the electronic structure of the superlattice.

To zeroth order, the low-energy exciton band structure in the moiré superlattice can be considered as a modification of the original TMD bands around the K and K' valleys. The large real-space periodicity generates a small reciprocal space periodicity, referred to as the moiré mini Brillouin zone (mBZ) (Fig. 2b). The moiré potential folds the original bands into the mBZ and opens a gap at the mBZ boundary. For large moiré superlattices, the width of the low energy bands

can be very small because of the small mBZ and the gap opening. These relatively flat bands can host interesting strong correlation effects, as will be discussed in detail later in this review.

Lattice relaxation and strain determine the final three-dimensional structure of the superlattice and the precise potential landscape. The variation in atomic stacking across the moiré unit cell leads to a position-dependent interlayer stacking energy[69,71–73]. To reduce the overall energy, the superlattice can relax and expand the regions of lowest energy. In a relaxed superlattice, domains of the energetically preferred stacking configuration form and are separated by a network of domain walls that accommodate lattice constant differences and twists. For homobilayers and same-chalcogen heterostructures (negligible lattice mismatch) at small twist angle (<2 deg), the moiré superlattice periodicity can be tens of nanometers[74–76] (Fig. 2c and 2d), exceeding domain wall widths and therefore allowing domains to fully form. The shape of the domains and the preferred stacking depends on whether the layers are stacked parallel (near 0 degrees) or antiparallel (near 60 degrees). At larger twist angles, homobilayer and same-chalcogen heterostructures form more ideal moiré superlattice structures without large domains[77]. Similarly, heterostructures formed by TMDs with different chalcogen atoms (large lattice mismatch) have a smaller moiré periodicity and tend to form more ideal moiré superlattices[8,67,78] (Fig. 2e). However, scanning tunneling microscopy of a WSe_2/WS_2 superlattice[79] demonstrated that heterostructures without large domains can still have large in-plane strain, causing 3D buckling of the layers and a resulting large moiré potential (Fig. 2f and 2g).

Hybridization of the electronic states from the two layers also influences the electronic structure in a moiré superlattice. Hybridization is particularly important in homobilayer superlattices, where the electronic states in each layer are degenerate. Here, states at Γ hybridize

strongly because the electron and hole wavefunctions extend out of the layer, while states at K hybridize less due to their confined wavefunctions and large spin-orbit coupling[37].

In this section, we describe how the moiré potential can localize excitons at different positions in the moiré superlattice, modify optical selection rules, and lead to emergent topological and correlated phenomena.

Intralayer moiré excitons

A long-period moiré pattern affects the dispersion of intralayer excitons via an effective moiré potential that mixes exciton states connected by the moiré reciprocal superlattice vector[66]. In a simple picture, the moiré potential arises because the band gap E_g of each layer depends on its local atomic displacement d relative to the other layer, which is a function of position r and varies smoothly with the moiré pattern. The spatial variation of exciton binding energy is small compared to the variation in the bandgap and can be ignored. The exciton potential energy can therefore be defined as $\Delta(r) = E_g(d(r)) - \langle E_g \rangle$, where $\langle E_g \rangle$ is the average of E_g over d. Fig. 3a shows *ab initio* calculations from Ref. 66 for an MoS_2/WS_2 heterobilayer near 0 degree twist angle, which suggests that the magnitude of the intralayer moiré potential is on the order of 10 meV. However, the value of the intralayer moiré potential depends strongly on the exact moiré structure considered, as described above.

Due to its periodicity, the moiré potential mixes exciton states that are separated by moiré reciprocal lattice vectors. Umklapp scattering off the moiré potential allows optical absorption and emission by the formerly dark finite-momentum exciton states. Consequently, the optical absorption peaks for intralayer excitons are split into multiple peaks by the moiré superlattice (Fig.

3b). Further, the excitons can be localized at different high symmetry positions in the superlattice, leading to complex absorption and emission spectra.

The splitting of intralayer exciton peaks has been observed experimentally in diverse moiré superlattice systems, including heterobilayers and homobilayers. In WSe_2/WS_2 heterostructures, Jin *et al.* revealed that the WSe_2 A exciton is split into three states separated by ~100 meV (Fig. 3c), which is consistent with a large moiré potential of ~250 meV that localizes intralayer exciton states at specific high-symmetry regions in the heterostructure[8]. When the heterostructure is doped with additional electrons, the three exciton states respond differently (Fig. 3d), which is consistent with both excitons and electrons being localized at specific positions in the superlattice. The large splitting has been reproduced in Ref. 14 and 80. Tang *et al.* also observed three intralayer exciton states separated by ~70 meV in a $MoSe_2/WS_2$ heterostructure[80]. The large splitting of intralayer exciton states shows that the moiré potential can be larger than predicted by *ab initio* calculations and that the exact structure and strain within the moiré superlattice is critical to determining its excitonic properties.

In a WSe_2/WSe_2 homobilayer, Andersen *et al.* combined SEM and photoluminescence (PL) measurements to demonstrate the emergence of a second exciton state in regions of the sample where the moiré periodicity is large (> 10 nm)[81] (Fig. 3e). In this system, two high-symmetry positions exist in the superlattice. The exciton state at the higher-energy position only emits if the state does not move to the lower energy position before radiative recombination. In regions with a large moiré periodicity, the distance that the exciton moves before recombining is smaller than the periodicity, so emission from the higher energy site emerges. Gate-dependent PL measurements demonstrate varying degrees of valley coherence for the different exciton species, depending on which layer the additional charge occupies and its momentum state. The observation

of localized moiré intralayer excitons in several moiré systems suggests that the moiré potential for intralayer excitons can be large and may dominate the exciton kinetic energy. Therefore, intralayer moiré excitons may be a powerful and interesting system for investigating correlated excitonic states.

Additionally, the electron-hole exchange interactions can lead to interesting topological properties of the intralayer moiré exciton bands[66]. As shown in Box 1, intervalley exchange interactions act on the valley pseudospin like an in-plane pseudo-magnetic field which rotates by 4π when the momentum encloses the origin once. With a valley Zeeman term that splits the degeneracy at the γ point, the exciton bands can have nonzero Chern number in the moiré mBZ. The valley Zeeman term has been experimentally realized in monolayer TMDs by applying a magnetic field[82–84] and by using a valley selective optical Stark effect[85,86]. Fig. 3f shows the intralayer moiré exciton band structure when a Zeeman field is applied and the corresponding Chern numbers of each band. The lowest exciton band has Chern number $C = +1$ and is separated from higher bands by a gap. Bulk-edge correspondence then implies the existence of chiral excitonic edge states as explicitly calculated and shown in Fig. 3g, where in-gap edge states appear in the energy spectrum for a stripe geometry. Importantly, these predictions hold for a wide range of moiré potential parameters. Unlike electronic bands whose topological properties imply quantized conductance, the bosonic nature and charge neutrality of excitons add subtlety to the experimental detection of band topology. For excitons, the existence of edge states can be detected by spatially resolved absorption spectroscopy.

Interlayer moiré excitons

A moiré superlattice also produces an effective potential landscape for interlayer excitons that can localize states within the superlattice and modify their emission and diffusion characteristics[7,11,87] . The moiré potential is defined similarly to the case of intralayer excitons, $\Delta(r) = E_g(d(r)) - \langle E_g \rangle$, but with E_g representing the interlayer band gap. Computed values of the interlayer moiré potential in twisted MoS_2/WS_2 bilayers at 0 degrees from Ref. 11 are shown in Fig. 4a. Interestingly, *ab initio* calculations predict that the depth of the interlayer moiré potential is much larger (on the order of 100 meV) for 0 degree stacks than for near-60 degree stacks (on the order of 10 meV). Calculations of the interlayer moiré potential in other TMD combinations predict similar values[7,88,89].

The relative twist between the two layers also shifts the electron and hole bands relative to each other in momentum space. As a result, when momentum is measured from the band extremum in each layer, the optically-active exciton states are not those with zero center-of-mass momentum, but those with finite momentum $\boldsymbol{Q} = (\boldsymbol{K}_B + \boldsymbol{G}_B) - (\boldsymbol{K}_T + \boldsymbol{G}_T)$, where $\boldsymbol{K}_B$ ($\boldsymbol{K}_T$) is the *K* valley in the Brillouin zone of the bottom (top) layer, and $\boldsymbol{G}_B$ ($\boldsymbol{G}_T$) is the reciprocal lattice vector in the bottom (top layer). The lowest excitation momenta of bright excitons are $\boldsymbol{q}_1 = \boldsymbol{K}_B - \boldsymbol{K}_T$ and its two C_3 partners defined as $\boldsymbol{q}_2$ and $\boldsymbol{q}_3$. The moiré potential mixes all the optically active exciton states because they are related to each other by moiré reciprocal lattice vectors.

The low-energy interlayer exciton states are typically localized at the high symmetry sites in the superlattice[7,11,87], which has important consequences for the optical selection rules of the excitons. At these positions, the local stacking registry is symmetric under C_3 rotations, so the exciton wavefunctions $|\chi\rangle$ must be eigenstates of C_3 rotation about its center and can be classified by $C_3|\chi\rangle = exp(i2\pi l_\chi/3)|\chi\rangle$ with $l_\chi = 0$ or ± 1. The excitation from the ground state of the heterostructure to the exciton state $|\chi\rangle$ is coupled to $\sigma\pm$ circularly polarized light if $l_\chi = \pm 1$, and

optically forbidden for normal incident light if $l\chi = 0$. Typically, the angular momentum, l_χ, is determined by the spin and valley indices, but in a moiré superlattice, the position of the exciton in the superlattice is also relevant. Depending on the specific high symmetry position, the electron and hole can have different rotation centers and their Bloch functions will have different eigenvalues, as shown in Fig. 4b, which leads to an additional angular momentum. Therefore, interlayer excitons at different high symmetry points can have different selection rules (Fig. 4c). This additional angular momentum can also brighten spin-forbidden dark states: in monolayer TMD, states with opposite electron and hole spins are optically dark (Fig. 4d), but in a moiré superlattice, the additional angular momentum can brighten the dark states and endow them with well-defined selection rules.

While intralayer excitons are easily studied via absorption spectroscopy due to their large oscillator strengths, interlayer excitons have relatively weak oscillator strengths because of the larger electron-hole separation and are commonly probed using emission measurements. Zhang *et al.* measured the polarization-resolved PL spectra of an aligned $MoSe_2/WSe_2$ heterostructure when pumped at the WSe_2 A exciton resonances[10] (Fig. 4e). The spectrum shows two main peaks with different helicities, which were assigned to interlayer excitons with the same and opposite spin at a single moiré superlattice potential minimum. In the same system, Joe *et al.* measured the effective g-factors of the interlayer exciton emission peaks, which are consistent with same and opposite spin states[90]. Because the interlayer excitons have out of plane dipole moments, their energy can be tuned with a vertical electric field. Using a dual-gated $MoSe_2/WSe_2$ sample, Ciarrocchi *et al.* applied an external electric field to tune the energy of the two interlayer excitons, along with their emission intensity and polarization[91] (Fig. 4f). The observation that the excitons shift together with

field indicates that they have the same dipole moment and are likely at the same moiré superlattice potential minimum[10,92].

Although PL is a sensitive probe, PL intensity depends on both the oscillator strength and the lifetime of a state. The latter depends sensitively on several sample-dependent factors, like defects and strain, which complicate the emission spectrum and have led to conflicting experimental results and interpretations[50,93–100]. To avoid this complication, Jin *et al.* used two background-free absorption techniques – PL excitation (PLE) and pump probe spectroscopies – to unambiguously determine the different contributions to theinterlayer exciton optical selection rules in a WSe_2/WS_2 moiré superlattice[12]. The authors observe only one peak in their low-temperature PL spectrum, which they assign to a single, low-energy interlayer exciton state. To observe higher energy interlayer exciton states, the authors varied the excitation energy and recorded the intensity of the PL emission, which is a direct measurement of the absorption at the excitation energy. The corresponding PLE spectrum in Fig. 4g shows two high energy resonances (labelled by green and yellow) with opposite helicities. Pump probe spectroscopy was then used to directly pump the interlayer exciton states and probe the valley state of holes in the superlattice, which provided information about the spin state of the interlayer excitons. The authors assigned the three observed states to same-spin and opposite-spin interlayer excitons localized at different high symmetry sites in the moiré superlattice.

At low excitation density, the strong moiré potential (~100meV in $MoSe_2/WSe_2$ case) can confine single excitons, forming an array of quantum emitters that can serve as single-photon emitters or sources of entangled photon pairs[9,101–103]. Fig. 4h shows the PL spectra of aligned $MoSe_2/WSe_2$ heterostructures at different excitation powers when exciting near the WSe_2 resonance[9]. When the excitation power is decreased from 10 uW to 20 nW, the broad interlayer

PL spectrum evolves into multiple narrow peaks. The average linewidth of around 100 ueV is comparable to those of defect-based quantum emitters reported in WSe_2 monolayers[104–107]. Li *et al*. also reported repulsive dipole-dipole interactions in these localized emitters and spectral jittering, indicating that the emitting states can belong to the same localizing potential well[101]. The uniformity and tunability of moiré-confined quantum emitters suggests great promise for quantum and nonlinear photonic applications.

Hybrid moiré excitons

In homobilayer moiré systems, the electron and hole wavefunctions are typically spread over both layers, leading to mixed interlayer and intralayer exciton states, often referred to as hybrid excitons[108–110]. These excitons have the characteristics of both an interlayer and intralayer exciton and are both electronically tunable and have appreciable oscillator strength. Scuri *et al.* use polarization-resolved and time-resolved PL to study interlayer exciton states in several twisted WSe_2/WSe_2 samples, including artificially-stacked (near 0 degree) and natural (near 60 degree) bilayers [110]. In all samples, the authors observed several emission peaks at lower energy than the direct K-K intralayer exciton transition, which they assigned to K-Q momentum indirect interlayer exciton states where the hole is localized in a single layer and the electron is delocalized between the layers. In samples with near 0 degree twist angle, they observed a high (>60%) degree of circular polarization in the interlayer exciton emission that can be tuned with electrostatic doping.

Heterostructures formed with different TMDs can also host hybrid exciton states. When bands in each layer of the heterostructure are close in energy and have the same spin, spin-conserving resonant tunneling of carriers between the layers can result in spatially mixed moiré excitons[111]. In $MoSe_2/WS_2$ heterostructures, the conduction bands of $MoSe_2$ and WS_2 have

similar energies, so the interlayer exciton formed by a hole in the valance band of $MoSe_2$ and an electron in the conduction band of WS_2 can hybridize with the $MoSe_2$ intralayer exciton (Fig. 5a). Alexeev *et al.* showed that new hybrid exciton states appear in both the absorption and PL spectra near the $MoSe_2$ A exciton when the two layers are aligned to near 0 and 60 degrees[112]. Zhang *et al.* observed hybrid states formed with both $MoSe_2$ A and B excitons and WS_2 A excitons[113]. They also showed that the twist angle provides a sensitive tuning knob of the properties of the hybrid moiré excitons (Fig. 5b). In particular, hybridization is enhanced as the moiré lattice becomes commensurate with the monolayer lattices at twist angles of 21.8 and 38.2 degree, where the K-valleys of the two layers become connected by moiré reciprocal lattice vectors. In the same system, Tang *et al.* identified two families of spatially entangled moiré excitons with very different effective electric dipoles (D ~ 0.24 and 0.17 e·nm)[80]. One plausible explanation for the large difference is that the interlayer exciton sates are localized at different moiré superlattice sites with different dielectric environments or degrees of wavefunction overlap.

In WSe_2/WS_2 moiré superlattices, the highest spin-split WS_2 valence band is nearly degenerate with the lower spin-split WSe_2 valence band (Fig. 5c). When the twist angle is near 60 degrees, these bands have the same spin, allowing for mixing of the WS_2 intralayer exciton with the interlayer exciton consisting of a hole in the WSe_2 valence band and an electron in the WS_2 conduction band. Tang *et al.* observed energy level anti-crossing as the interlayer exciton energy is tuned across the intralayer exciton energies by an electric field[80] (Fig. 5d), directly probing the hybridization.

Hybrid excitons have also been reported in many other heterostructures, including $MoSe_2/MoSe_2$[114], $MoSe_2$/hbn/$MoSe_2$[115], MoS_2/WS_2[116], and $MoSe_2/WSe_2$[116]. For example,

Shimazaki *et al.* measured the electric field dependence of the PL and absorption of $MoSe_2$/hbn/$MoSe_2$ heterostructures[115] and observed coherent hole-tunneling-mediated avoided crossings of an intralayer exciton with three interlayer exciton resonances in the system. With large oscillator strength and high electric field tunability, the hybrid excitons in many heterostructure systems hold great potential for optoelectronic applications.

Correlated electronic states probed by excitons

Like excitons, single particle electronic states are also strongly modified by a moiré superlattice. The low-energy electronic degrees of freedom in a long-period moiré superlattice can be accurately described by a continuum model[117]. For TMDs, the low-energy degrees of freedom are electrons and holes moving in an effective moiré potential. To minimize the number of degrees of freedom, it is convenient to consider the valence bands of TMDs, where the spin splitting is large due to strong spin-orbit coupling[35]. Then in the hole-doped regime, we obtain the moiré band Hamiltonian $H_0 = -\frac{\hbar^2 \boldsymbol{k}^2}{2m^*} + \Delta(\boldsymbol{r})$ with two-fold valley degeneracy, where the first and second terms are the moiré band kinetic and potential energies, respectively. For a moiré potential with period a_M, the Wannier functions associated with the highest-energy moiré band are localized around the moiré potential maximum with spatial extension $a_W \sim a_M^{1/2}$. Since the ratio a_W/a_M scales as $a_M^{-1/2}$, the overlap between Wannier functions decreases as the twist angle decreases and as a result the moiré band flattens. In this limit, the isolated moiré band can be described by a tight-binging Hamiltonian

$$H_0 = \sum_{\boldsymbol{R},\boldsymbol{R}',\tau} t(\boldsymbol{R}' - \boldsymbol{R}) c^\dagger_{\boldsymbol{R}'\tau}\, c_{\boldsymbol{R}\tau},$$

where $\boldsymbol{R}$ and $\boldsymbol{R}$' represent sites on the triangular lattice formed by the moiré potential maximum points, and τ is the valley index. The moiré band dispersion is shown in Fig. 6a for a twisted $MoSe_2/WSe_2$ heterostructure, keeping up to the third nearest neighbor hopping terms[68]. The hopping parameters decay exponentially as the moiré periodicity increases, so the moiré miniband flattens for a larger superlattice.

In the small twist angle limit, hopping between moiré superlattice sites is weak and the Coulomb interaction between electrons becomes important. The onsite Coulomb repulsion energy $U_0 \sim e^2/\epsilon a_W \sim a_M^{-1/2}$ decreases slowly with the moiré period. The ratio of U_0 and the bandwidth ~ t then increases rapidly as the twist angle is reduced. At small twist angles, U_0 can be larger than the bandwidth, so the system is dominated by interactions and is expected to show strong correlation effects like Mott insulator and quantum spin liquid states. In particular, the isolated hole band can be mapped to the single-band Hubbard model on a triangular lattice, which is expected to host a large range of exotic electronic states.

Correlated physics in moiré superlattices was first seen in twisted bilayer graphene and trilayer graphene/hBN samples, where observations of correlated insulating states and superconductivity delighted the field[118,119]. However, TMD moiré superlattices have several distinctions and advantages. First, TMDs are predicted to exhibit very strong correlation effects because of their moderate effective masses (m_e^* ~ 0.3-0.5 m_0) relative to single and few-layer graphene. With larger effective mass, the bands of the constituent layers are already much flatter than in single and few-layer graphene, leading to even flatter bands in the superlattice. Second, the spin/valley optical selection rules give direct access to the spin degrees of freedom in TMDs, providing an opportunity to investigate spin structures in the correlated states.

Although correlated insulating states are commonly probed via transport measurements, the large contact resistance in TMD devices[120] has shifted attention towards optical approaches. Excitons are extremely sensitive to the local charge density[121,122] and dielectric environment[48], which makes it possible to probe electronic states using excitons. So far, much of this work has focused on WSe_2/WS_2 moiré superlattices, where a huge variety of correlated electronic states have been observed using various exciton probes.

Regan *et al.* implemented a novel technique, optically-detected resistance and capacitance, in which the WSe_2 excitonic absorption was used to measure charge transport between two regions in a WSe_2/WS_2 moiré superlattice under a small modulation voltage[13]. The authors observed a strong gap-like feature when the sample was doped to half filling (one hole per moiré unit cell, $n = n_0$), which is consistent with a Mott insulator described by a Hubbard model with on-site interactions (Fig 6b,c). They also saw gaps at $n = n_0/3$ and $2n_0/3$, which were assigned to generalized Wigner crystallization on the superlattice due to strong interactions between electrons on neighboring superlattice cites. The observation of generalized Wigner crystallization confirms that correlations are particularly strong in the TMD moiré superlattices and that long-range Coulomb interactions are large. Tang *et al.* also observed the insulating state at $n = n_0$ via an enhancement in the WSe_2 exciton absorption that is likely due to reduced free scarier screening of the electron-hole interaction in the insulating state[14].

More recently, Xu *et al.* found that the excitons in a monolayer TMD layer placed ~ 1 nm away from a TMD moiré superlattice can be sensitive probes of the electronic states in the superlattice[15]. In particular, the electron-hole separation in exciton excited states (2s, 3s, etc.) is much larger than the TMD monolayer thickness, and the bound state is therefore strongly influenced by the local dielectric environment, including the nearby moiré superlattice. By

monitoring the 2s state in a monolayer WSe_2 sensor layer, the authors observed more than a dozen insulating electron and hole states in a WSe_2/WS_2 moiré superlattice, which correspond to specific electron and hole configurations on the underlying superlattice (Fig. 6d). The temperature dependence of this effect revealed that correlations are stronger on the electron side, where the states persist to higher temperatures. The authors propose that some of the newly observed states at fractional filling could be charge density wave analogues of the states at $n = n_0/3$ and $2n_0/3$ or pair density waves. Further theoretical and experimental studies will be required to determine the nature of all these states.

Exciton probes of magnetic structure and electronic anisotropy have been used to further advance understanding of the correlated states in the WSe_2/WS_2 moiré superlattice. Tang *et al.* measured the helicity-resolved absorption of the WSe_2 exciton as a function of the out-of-plane magnetic field, where the observed exciton Zeeman splitting is influenced by both the applied field and the magnetic moments of the localized holes[14]. With this technique, they observed antiferromagnetic behavior at half filling of the superlattice followed by a transition to a weak ferromagnetic state at higher doping (Fig. 6e). Jin *et al.* performed combined optical anisotropy and electronic compressibility measurements to show that some of the correlated states at fractional filling of the superlattice are linear or zigzag striped phases characterized by spontaneous rotational symmetry breaking[123] (Fig. 6f). The electronic anisotropy induces a polarization rotation in incident linear polarized light, and the response is enhanced by choosing a photon energy resonant with the WSe_2 exciton. By imaging the stripe domains, the authors conclude that the charge stripes are preferentially aligned along the high symmetry axes of the superlattice.

While most investigations have focused on the WSe_2/WS_2 superlattice, correlated physics has also been studied in other moiré systems, including WSe_2 homobilayers[77,124] and $MoSe_2$

homobilayers where the $MoSe_2$ layers are separated by a thin hBN layer[115,125]. In the latter case, the moiré period is not limited by the lattice mismatch and can be very large, but the moiré potential is suppressed by the hBN spacer. Using different combinations of TMDs with and without spacers, the moiré potential can be engineered to access regimes where strong correlations exist, but also where the Coulomb energy and bandwidth compete. In these diverse systems, excitons are powerful probes of correlated insulating states, magnetic and spin structure, and anisotropy.

Section 3: Excitons in Cavities

TMD excitons coupled to a cavity

Controlling and enhancing interactions between light and matter is essential for constructing integrated photonic devices, which use light to efficiently store and process information. One method of controlling light-matter interaction is by using a cavity, which can enhance the emission rate and modify the electronic energy levels of the optically active media. TMDs present new opportunities for making efficient photonic and optoelectronic devices with a valley degree of freedom that can be easily integrated with existing silicon-based photonics[16–18]. Monolayer TMDs host intralayer excitons that have a large oscillator strength and interact strongly with light, so they are good candidates for studying part-light, part-matter exciton-polariton quasiparticles[126–134] and their interesting quantum many-body phenomena such as Bose-Einstein condensation.

As described above, TMD heterostructures can host a variety of exciton states, including interlayer excitons, which have smaller oscillator strength compared to intralayer excitons and thus interact weakly with light. However, interlayer excitons are longer-lived and have strong dipole-dipole interaction strength, which could facilitate the realization of collective many-body

phenomena such as exciton condensation and superfluidity[51,135,136]. Furthermore, moiré superlattices in heterostructures provide additional degrees of freedom for excitonic band structure engineering, and the out-of-plane dipole moment of interlayer excitons allows for easy electrical tuning of exciton properties and electrical injection of carriers[58,59,80,137]. Therefore, cavity integrated TMD heterostructures provide an exciting platform for observing collective and controllable excitonic phenomena[138,139].

Interlayer excitons coupled to a cavity

The interaction between cavity photons and emitters underlies many fundamental observable processes, including spontaneous emission, stimulated emission, and quantum many-body phenomena. The strength of the interaction determines how strongly the excitons couple to the cavity modes. Here, we consider the enhancement of spontaneous and stimulated emission in the weak coupling regime as it pertains to TMD interlayer excitons.

In the weak coupling regime, the exciton-photon interaction strength is a small perturbation in the Hamiltonian, modifying the local density of states and the decay rates. One well-studied effect is the Purcell effect, which is the modification of spontaneous decay rates when the cavity mode is resonant with the emission energy. With sufficient cavity quality factor and light-matter interaction strength, the spontaneous emission rate can be enhanced by a factor defined as

$$F_P = \frac{3}{4\pi^2}\left(\frac{\lambda}{n}\right)^3 \frac{Q}{V},$$

where λ is the wavelength of light, n is the refractive index of the cavity, Q is the cavity quality factor, and V is the cavity mode volume.

Rivera et al. demonstrated Purcell enhancement in TMD heterobilayer interlayer excitons coupled to a gallium phosphide (GaP) photonic crystal cavity (Fig. 7a), with a 15-fold increase in

the photoluminescence intensity (Fig. 7b) and a simulation estimated Purcell enhancement factor of 60 (Ref. [140]). In this study, the gain medium was a $WSe_2/MoSe_2$ heterobilayer which hosts long-lived interlayer excitons. The cavity was a photonic crystal defect cavity made with high index GaP, which can have small mode volumes and large quality factors, making them ideal for energy efficient photonic devices. This experiment set the foundation for studying cavity quantum electrodynamics (QED) effects in 2D heterostructure nanophotonics.

Another interesting opportunity lies in the engineering of emission rates to achieve heterostructure-based lasers. Spontaneous emission occurs when the carriers in the excited state relax down to the ground state while emitting light. In this case, the carrier population of the ground state (N_1) is larger than the carrier population of the excited state (N_2), and the resulting emitted light is incoherent. Stimulated emission, however, occurs when gain in the material overcomes cavity losses and carrier population is inverted ($N_2 > N_1$). The resulting emission is amplified and both spectrally and spatially coherent. Stimulated emission is the mechanism of light amplification in lasers.

TMD heterobilayer interlayer excitons provide opportunities for compact, integrable, tunable, valley polarized semiconductor lasers. Choosing the appropriate combination of monolayers can result in a bilayer with a type-II band alignment, which allows for carrier pumping through the intralayer exciton resonance, followed by ultrafast charge transfer to the lower energy bands. This allows efficient carrier build-up and population inversion while avoiding carrier losses due to intralayer exciton radiative emission. Additionally, with precise rotational alignment of the crystal axes of the layers, the interlayer exciton forms a direct band gap with sufficient oscillator strength for lasing, and the layers can form moiré superlattices that can modify the potential landscape and further localize the interlayer excitons and enhance the radiative decay rate into the

lasing mode. Lasing in TMD heterobilayers have been demonstrated by Liu et al. (Ref. 141) and Paik et al. (Ref. 142), using a photonic crystal cavity and one dimensional (1D) grating resonator cavity, respectively. Liu et al. demonstrated room temperature laser operation indicated by a super-linear increase in emission intensity and a decrease in linewidth at the threshold pump power, which signifies increased phase coherence (Fig. 7c-e). Paik et al. observed a sharp increase in spatial coherence length above threshold pump power, which indicates the formation of extended spatial coherence (Fig. 7f-h). These studies open the door for energy efficient, electrically injected, room temperature semiconductor nanolasers that are easily integrable with existing silicon-based photonics.

In heterobilayers, intralayer exciton can split into multiple exciton species as a result of moiré confinement[8] or interlayer hybridization[113]. These moiré exciton arrays exhibit large oscillator strength in the same order of magnitude as the monolayer exciton and, thanks to the uniformity of the moiré lattice, inhomogeneous broadening comparable with the radiative linewidth. By integrating a $WS_2/MoSe_2$ heterobilayer with a planar Fabry-Perot cavity, Zhang et al. demonstrated a moiré exciton polariton system with cooperative coupling between an array of zero dimensional (0D) moiré excitons and microcavity photons[143]. The moiré polaritons exhibited strong nonlinearity due to exciton blockade, suppressed exciton energy shift, and suppressed excitation-induced dephasing, all of which are consistent with the quantum-confined nature of the moiré excitons. The system therefore introduces quantum-dot like nonlinearity into cooperatively coupled solid state system, opening a door to novel quantum many-body physics and polariton devices.

Section 4: Outlook

Exciton physics in TMD heterostructure systems is enriched by moiré modulation, which creates excitonic minibands that split absorption and emission peaks and improves the phase space available to decoherence processes, and by large binding energies that allow interlayer excitons to be experimentally accessible even when the two TMD layers are widely separated. Among the large number of exciting possibilities opened up by these properties, several of which are highlighted below, only a few have already been explored in any depth.

Interlayer exciton condensation

The possibility of Bose-Einstein condensation of excitons has been recognized[144,145] since the 1960s. However, the experimental realization of unambiguous exciton condensation in bulk materials has been quite challenging. One major obstacle has been the short lifetimes of optically generated excitons, which can in principle be mitigated[146–151] by separating the electrons and holes into different layers so that their optical recombination times are increased. Spatial separation between electrons and holes also ensures a repulsive dipolar interaction between excitons and prevents the formation of biexcitons.

TMD heterostructures have now added an important new wrinkle to spatially indirect exciton physics by allowing the electron and hole separation to be extended by inserting several intermediate layers of resistive hexagonal boron nitride (hBN), extending optical lifetimes by orders of magnitude, all while maintaining sizable electron-hole binding energies. The exciton binding energy is important because it sets an upper limit on the condensation temperature[135,152,153]:

$$k_B T_C \sim \frac{\pi \hbar^2 n_x}{2m_x} \lesssim 0.1 E_{xb} .$$

Here $m_x = m_e + m_h$ and n_x are the exciton mass and density, and E_{xb} is the spatially indirect

exciton binding energy. The intermediate form for $k_B T_C$ applies if the superfluid fraction is close to unity near the transition[154], whereas the final form is an approximate upper bound that applies close to the crossover between the condensed boson (BEC) and itinerant electron hole pair (BCS) limits.

Because excitons are normally relatively high energy elementary excitations, they are present in equilibrium only in finely tuned materials in which E_{xb} exceeds the band gap. Although this condition can be achieved in graphene multilayers[155–157], it cannot be satisfied in TMD heterostructures. Excitons must instead be generated by electrical or optical excitation. In TMD heterostructures, a bias voltage applied between layers can act[158,159] as an exciton reservoir, as illustrated in Fig. 8. Quasi-equilibrium fluids of spatially indirect excitons have very recently been established in TMD heterostructures[160] via this mechanism, opening up opportunities to study exciton transport and achieve electrical control of light. The spectacular electrical properties of quantum Hall exciton condensates[161–164] provide a sense of what might be achievable.

Boson Hubbard model and superfluid insulator transition with moiré excitons

Because of a transition from superfluid to insulator that occurs in the narrow band limit, the quantum physics of equilibrium bosons is richer in lattice systems[165,166]. As explained above, equilibrium indirect exciton systems can be achieved in TMD heterostructures by separating electron and hole layers with a hBN barrier. It remains to be seen whether sufficiently narrow exciton bands can be formed when a moiré pattern is present. Moiré modulation potentials in TMD heterostructures arise partly from level repulsion with neighboring layers, and partly from electrostatics[167]. When the electrons and holes that form the indirect exciton are separated by a hexagonal boron nitride barrier, both components of the moiré potential are strongly attenuated,

and new routes may need to be found to achieve modulation. One possibility is to employ an intermediated twisted graphene bilayer that is electrostatically doped.

Moiré exciton polaritons

In heterostructures with a type-II band alignment, the long valley lifetime and long diffusion length of interlayer excitons, together with the flexibility of tuning the doping levels of 2D materials, may facilitate the realization of ultra-compact and integrated electro-optical devices[58,59]. In the development of 2D material lasers[142], future studies may clarify the optimal band structures and the role of carrier localization in moiré lattices using different combinations of monolayer materials with varying twist angles.

In heterostructures with type-I band alignment or strong inter- and intra-layer exciton mixing, the tunability of moiré excitons, via doping, electric field, and twist angle, are transcribed to the moiré polaritons[143]. Uniquely, tuning interlayer hybridization provides a way to tune the exciton-photon coupling strength, exciton-photon detuning, and nonlinearity[168–170] of the polariton modes. Such polariton systems promise broad tunability, high operating temperature, and ready integration in diverse material platforms.

Incorporation of moiré lattices leads to a new type of polariton system whose properties are yet to be studied and understood. Further understanding and control of the anomalously strong nonlinearity of moiré polaritons at low density may open a new pathway to polariton blockade [171–174] and ultralow power nonlinear optical switches[175]. Interplay between moiré lattice potential and photonic potentials may open new opportunities in cavity-control of electronic phases[176–179].

Hybrid systems

2D materials are allowing physical scientists to play god in surprising new ways, and exciton physics seems certain to play a central role. The range of possibilities is greatly expanded when we consider employing TMD heterostructure exciton fluids as one component of multi-physics hybrid systems. For example, as mentioned above, an electrostatically-doped twisted graphene bilayer could be placed between TMD heterostructure bilayers containing exciton fluids. Because the graphene bilayer can have an enhanced density-of-states when twisted and density-fluctuations of the TMD heterostructure fluids can[180,181] mediate pairing, relatively high temperature superconductivity seems a likely result. This is one example among many. The prospects for exciton and exciton-polariton physics in TMD heterostructures are bright indeed.

Figures:

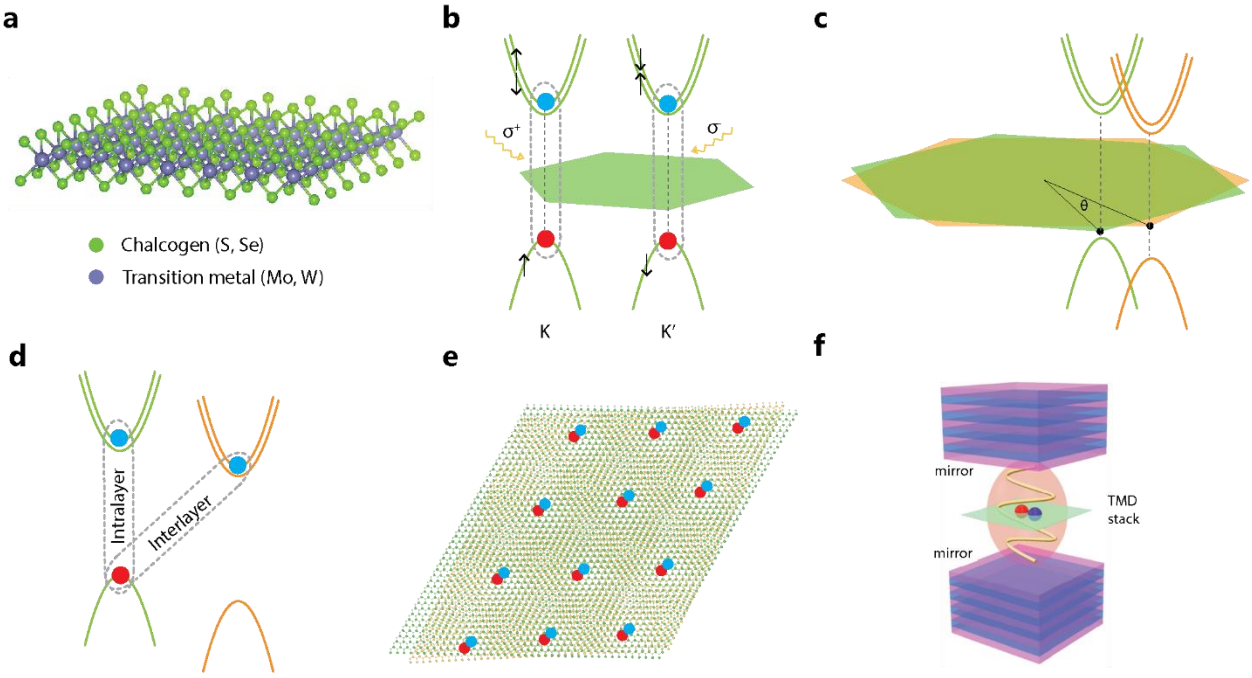

Figure 1 | **Excitons in TMD heterostructures. a.** | Structure of 2H TMD monolayer with chalcogen (S, Se) in green and transition metal (Mo, W) in purple. **b.** | Schematic of the bright excitons and the K and K' corners of the Brillouin zone (hexagon) of a TMD monolayer. Excitons at the K (K') valley couple to σ+ (σ-) light. **c**. | Schematic of a heterostructure formed by two TMDs (green and orange) in momentum space. The heterostructure is characterized by the lattice mismatch, twist angle (θ), and band alignment between the two layers. **d**. | Schematic of intralayer and interlayer excitons at the K valley of two layers forming a heterostructure with type II band alignment. **e**. | A twist angle or lattice mismatch in a heterostructure leads to the formation of a moiré superlattice, where excitons can be localized at specific positions in the superlattice unit cell. **f**. | Schematic of a TMD heterostructure in an optical cavity, which can dramatically modify the exciton properties. Panel **f** adapted from Ref. [182].

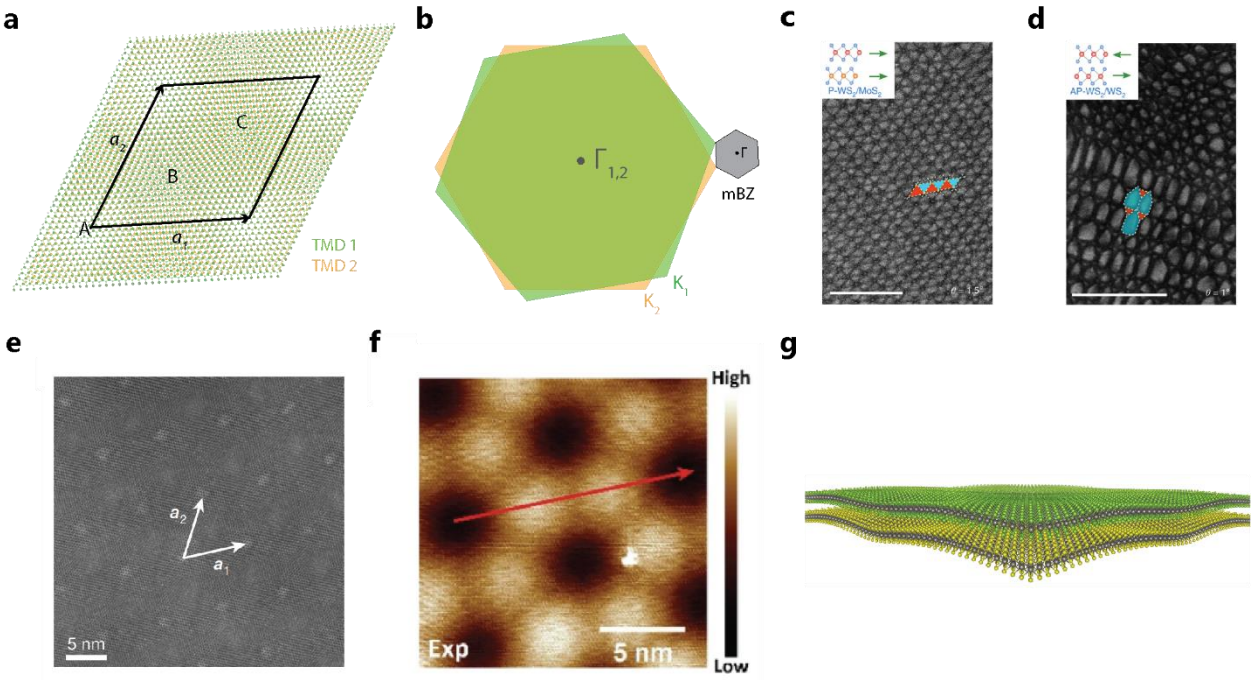

Figure 2 | **TMD moiré superlattices. a**. | Illustration of a moiré superlattice formed by two TMDs in real space. The superlattice vectors are labelled as $\boldsymbol{a}_1$ and $\boldsymbol{a}_2$ and form the superlattice unit cell. A, B, and C mark the high-symmetry positions in the superlattice where the local atomic configuration has three-fold rotational symmetry. **b**. | Schematic of the Brillouin zones of each monolayer (green and orange) and the mini Brillouin zone (mBZ) of the superlattice, where the mBZ wavevector corresponds to the difference between the two K points of the monolayers. **c**. and **d**. | Annular dark-field scanning transmission electron microscope (STEM) images of the domain structures in a (**c**) 1.5-degree twist angle WS_2/MoS_2 heterostructure and a (**d**) 59 degree twist angle WS_2/WS_2 heterostructure. Scale bar, 100 nm. The insets show schematics of the two layers with parallel (P) or anti-parallel (AP) stacking. Red and blue regions highlight different domain types in each sample. **e**. | Atomic-resolution high-angle annular dark-field STEM images of a near-zero twist angle WSe_2/WS_2 heterostructure showing a moiré superlattice with superlattice vectors $\boldsymbol{a}_1$ and $\boldsymbol{a}_2$. **f**. | Scanning tunneling microscope image (Vbias = -0.19V. I = 100pA) of a graphene-covered WSe_2/WS_2 heterostructure showing the height variation across the moiré superlattice. **g**. | 3D illustration of the reconstructed WSe_2/WS_2 moiré superlattice. Panels **c** and **d** are adapted from Ref. 74, panel **e** is from Ref. 8, panels **f** and **g** are from Ref. 79.

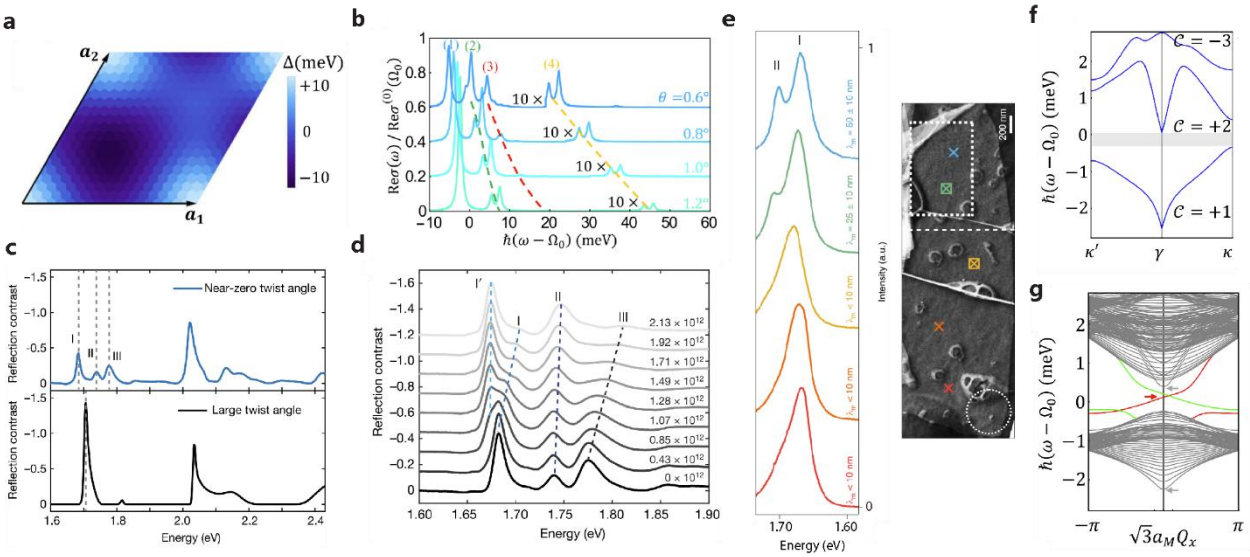

Figure 3 | **Intralayer moiré excitons a**. | Simulated variation of the MoS_2 bandgap in a zero-degree MoS_2/WS_2 bilayer. **b**. | Calculated optical conductivity of MoS_2/WS_2 heterostructure at several twist angles, θ, from 0 degrees. The curves are shifted vertically for clarity, and the dashed lines track the peak evolution. **c**. | Experimental reflection contrast (absorption) spectrum a near-zero-degree twist angle WSe_2/WS_2 heterostructure (blue, top) compared to a large twist angle WSe_2/WS_2 heterostructure (black, bottom). The WSe_2 A exciton in the large twist angle device (~1.7 eV) is split into three prominent peaks moiré exciton states (labelled I, II, and III) in the near-zero-degree twist angle device. **d**. | Reflection contrast spectra of a near-zero-degree twist angle WSe_2/WS_2 heterostructure when the device is electrostatically doped with electrons. The electron concentration, in units of cm^{-2}, is noted for each spectrum, and the spectra are offset for clarity. **e**. | Left: Photoluminescence spectra collected from a WSe_2/WSe_2 heterostructure at the positions noted by crosses with the same color in the scanning electron microscope image (right). The spectra are offset vertically for clarity. The amplitude of peak I (II) decreases (increases) with growing superlattice wavevector across the sample. **f**. | Low-energy exciton band structure of MoS_2/WS_2 bilayer with 1 degree twist from AB stacking and a Zeeman field hz = 1.5 meV. Each band is labeled by its Chern number C, and the gray bar shows the band gap. **g**. | Quasi-1D band structure of a stripe geometry for the same system, where the red and green curves show the chiral excitonic edge states. **a**, **b**, **f**, and **g** are from Ref. 66, panels **c** and **d** are from Ref. 8, and panel **e** is adapted from Ref. 81.

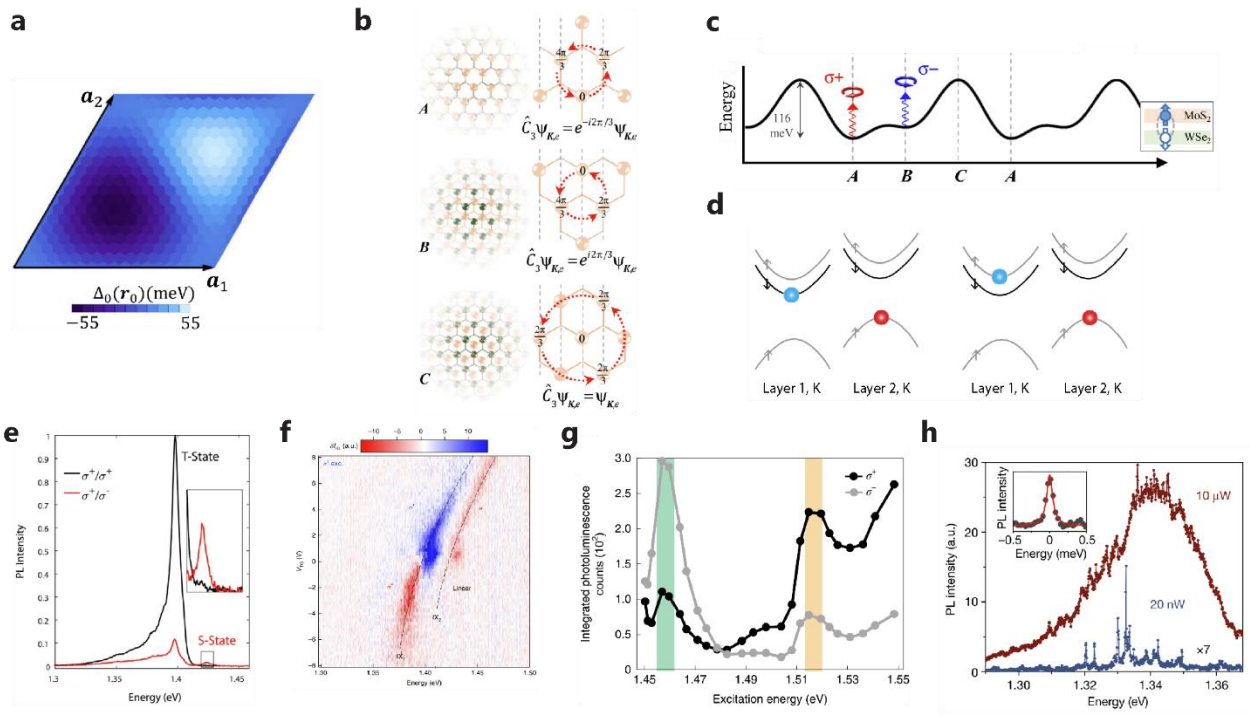

Figure 4 | **Interlayer moiré excitons a**. | Simulated variation of the interlayer bandgap in a zero-degree MoS_2/WS_2 heterobilayer. **b**. | Left: Schematic of exciton wavepackets at positions A, B, and C in the moiré superlattice unit cell, see Fig. 2a. Right: Corresponding transformation of the electron Bloch wavefunction $\psi_{\mathbf{K},e}$, when the rotation center is fixed at the hexagon center in the hole layer. Red arrows show the phase change by C3 and dashed lines show planes of constant phase. **c**. | Simulated potential landscape for interlayer excitons in a MoS_2/WSe_2 heterostructure, with optical selection rules for the spin-up excitons shown at the energy minima. **d**. | Interlayer exciton spin configurations at the K valley for a type II heterostructure made of tungsten materials, such as WSe_2/WS_2. The left (right) set of bands shows the opposite (same) spin exciton. **e**. | Photoluminescence (PL) spectra of a $MoSe_2/WSe_2$ heterostructure when exciting at the WSe_2 A exciton resonance with σ+ polarization, showing a large difference between the σ+ (black) and σ- (red) emission. Two peaks, labelled S-state and T-state, have opposite helicity and correspond to the same and opposite spin states, respectively. The inset shows a zoom-in view of the S state. **f**. | PL map of the difference between right (σ+) and left (σ+) circularly polarized emission intensities of the two interlayer exciton states, labelled IX_1 and IX_2, when the $MoSe_2/WSe_2$ device is pumped with right (σ+) circularly polarized light, $\delta I_{RL}=I_R - I_L$, as a function of the gate voltage. The emission polarization is gate-tunable. **g**. | PL excitation spectrum showing integrated σ+ (black) and σ+ (grey) PL counts when a WSe_2/WS_2 heterostructure is pumped with σ+ light, showing enhanced emission when the light is resonant with two interlayer exciton states highlighted in green and yellow. These states correspond to same spin interlayer excitons at two high symmetry positions in the superlattice unit cell. **h**. | Comparison of the PL spectra from a 2-degree twist angle $MoSe_2/WSe_2$ heterobilayer when exciting with 10 uW (dark red) and 20 nW (blue, intensity scaled by 7x). Inset shows Lorentzian fit to a representative PL peak from the 20 nW spectrum, showing a linewidth of approximately 100 μeV. Panel **a** is from Ref. 11, panels **b** and **c** are from Ref. 7, panel **d** is adapted from Ref. 12, panel **e** is from Ref. 10, panel **f** is from Ref. [91], panel **g** is from Ref. 12, and panel **h** is from Ref. 9.

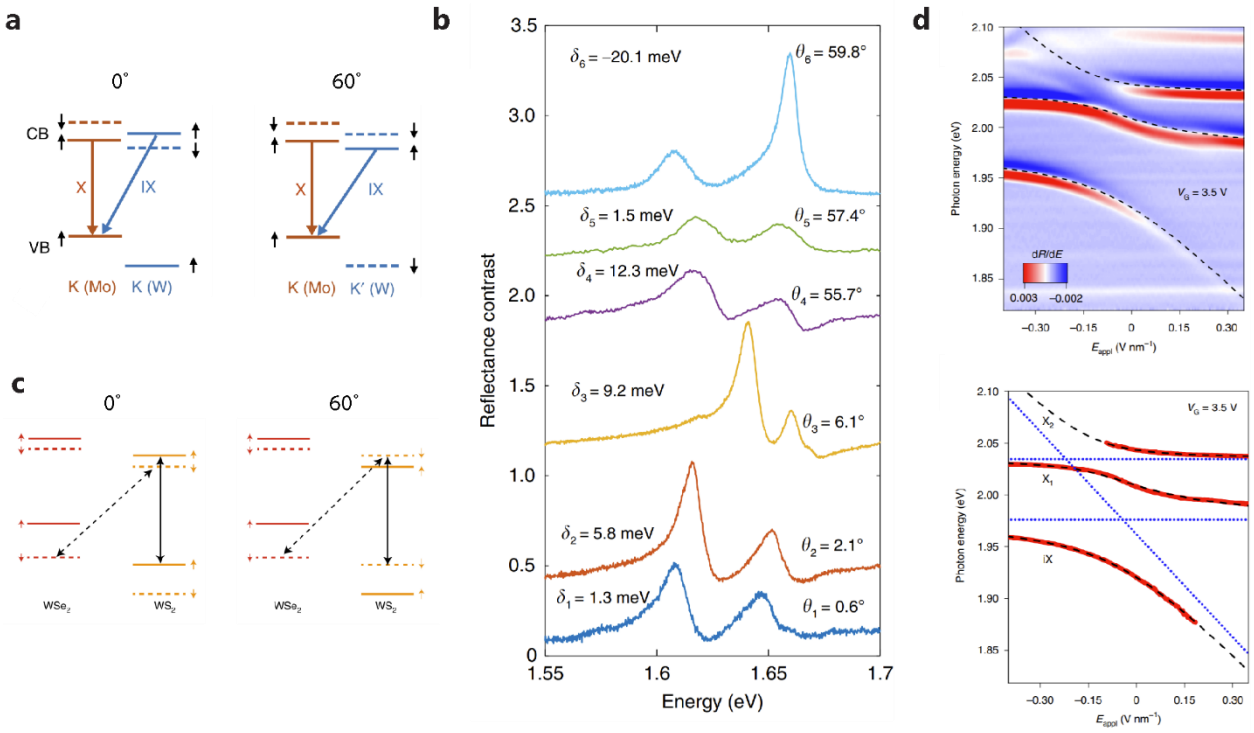

Figure 5 | **Hybrid moiré excitons a**. | Band alignment in 0 degree and 60 degree $WS_2/MoSe_2$ heterostructures, where spin up (down) bands are denoted by solid (dotted) lines. X labels the intralayer exciton transition and IX labels the nearly resonant interlayer excitation transition that shares the same hole state. **b**. | Reflection contrast spectra of $WS_2/MoSe_2$ heterostructures with various twist angles, θ_i, for $i = 1$–6. The spectra are shifted vertically for clarity. The extracted peak detuning $\delta_i = E_{IX,i} - E_{X,i}$ are labeled for each spectrum. **c**. | Band alignment in 0-degree and 60-degree WSe_2/WS_2 heterostructures, where spin up (down) bands are denoted by solid (dotted) lines. Solid (dashed) double-headed arrows show the dipole-allowed intralayer (interlayer) exciton transitions. The spin configuration in the 60-degree heterostructure allows for mixing of the intralayer and interlayer states. **d**. | Upper: Energy derivative of the reflection contrast spectrum of a 60-degree WSe_2/WS_2 heterostructure as a function of the out-of-plane electric field at a fixed doping density showing anti-crossing of exciton states. The dashed lines are the best fit to a three-level model. Lower: Electric field dependence of the extracted exciton resonance energies. Panels **a** and **b** are adapted from Ref. [113], and panels **c** and **d** are adapted from Ref. 80.

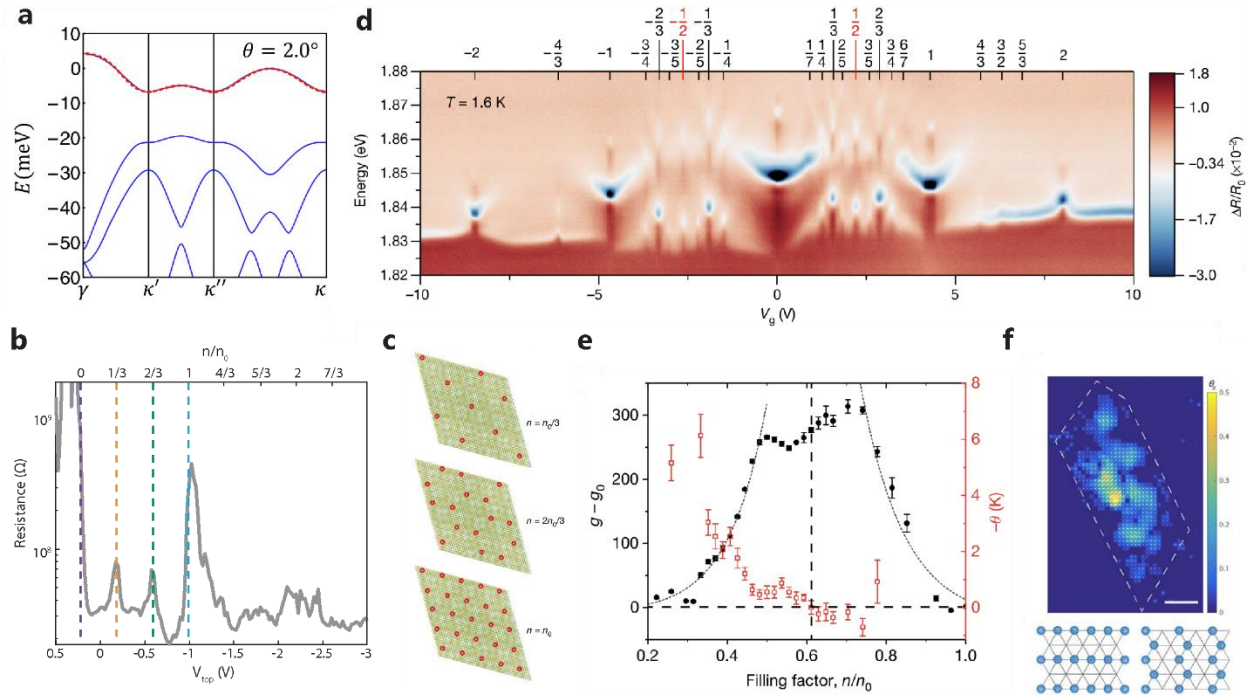

Figure 6 | **Excitonic probes of correlations in moiré superlattices a**. | Calculated electronic moiré bands for a 2-degree twist angle $MoSe_2/WSe_2$ moiré superlattice. The red dashed line is a tight-binding model fit to the highest valence band, including hopping up to the third nearest neighbor. **b**. | Resistance of a WSe_2/WS_2 moiré superlattice from charge neutral to moderate hole doping, measured via the optically detected resistance and capacitance technique. Enhanced resistance is observed at hole doping of $n = n_0/3$, $n = 2n_0/3$, $n = n_0$, where n_0 is one hole per moiré unit cell. **c**. | Corresponding illustration of the generalized Wigner crystal ($n = n_0/3$, $n = 2n_0/3$) and Mott insulator states ($n = n_0$). **d**. | Doping-dependent reflection contrast spectrum of the 2s exciton state in a sensor WSe_2 layer reveals many insulating states in a nearby WSe_2/WS_2 moiré superlattice at 1.6 K. The top axis shows the proposed filling factor for the insulating states, where 1 corresponds to one electron per moiré unit cell. **e**. | Magnetic susceptibility (left axis, black symbols) and Weiss constant (right axis, red symbols) of a WSe_2/WS_2 moiré superlattice as a function of the moiré filling factor, where n_0 corresponds to two holes per moiré unit cell. The black dotted lines (guide to the eye) indicate the divergent susceptibility at filling factors near 0.6. **f**. | Upper: Optical anisotropy mapping of a WSe_2/WS_2 moiré superlattice at a filling of one electron per moiré unit cell, revealing domains of electronic stripes. The length and orientation of the line segments at each point indicate the local amplitude and orientation of the anisotropy, and the color corresponds to the amplitude. Lower: two possible charge orders with linear and zigzag stripe. Panel **a** is from Ref. 68, panel **b** and **c** are adapted from Ref. 13, panel **d** is from Ref. 15, panel **e** is from Ref. 14, and panel **f** is from Ref. 123.

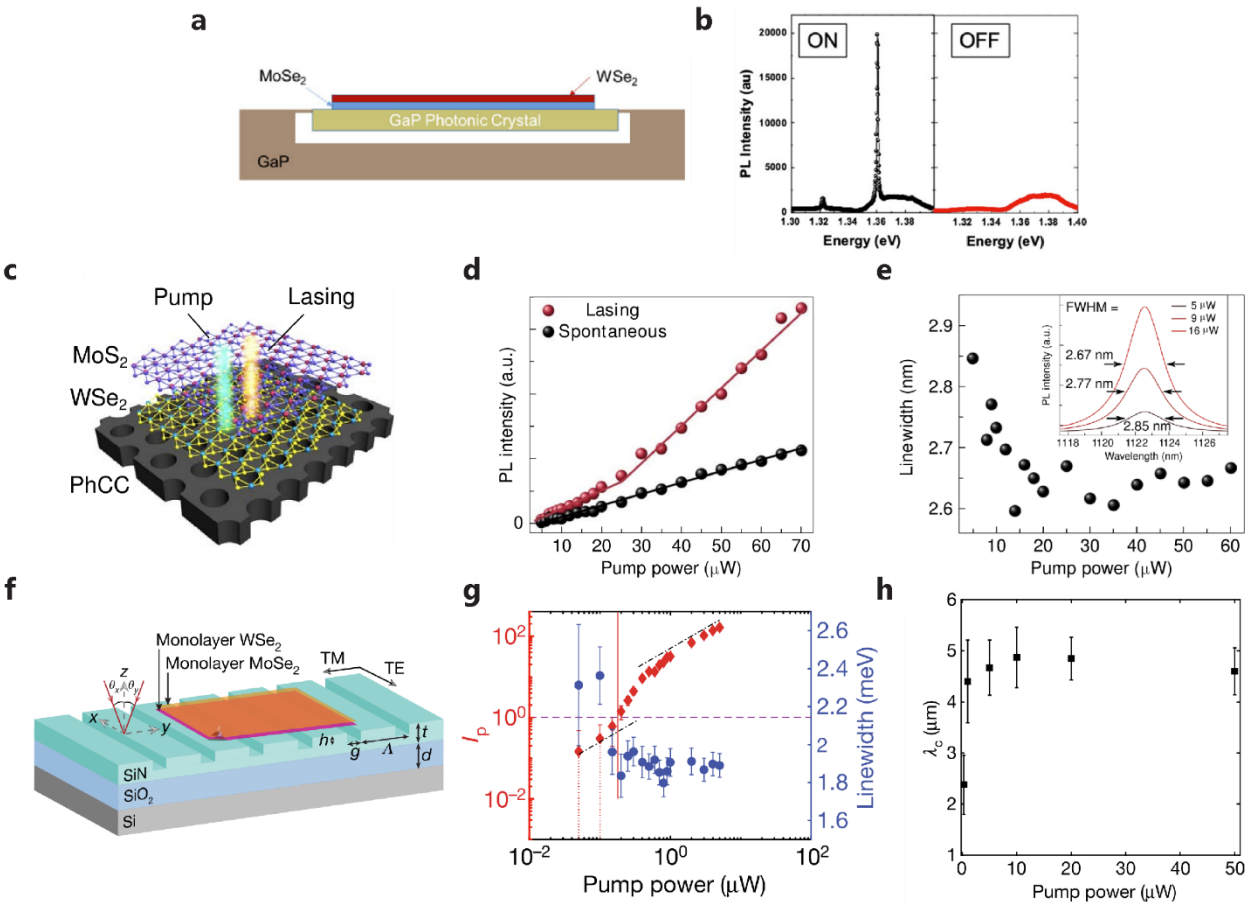

Figure 7 | **Excitons in optical cavities a**. | Schematic of a $MoSe_2/WSe_2$ heterostructure placed on top of a GaP photonic crystal. **b**. | Photoluminescence (PL) spectra from the $MoSe_2/WSe_2$ heterostructure on (left) and off (right) the linear three-hole defect cavity in the photonic crystal. **c**. | Illustration of a nano-laser formed from a MoS_2/WSe_2 heterostructure on a photonic crystal cavity. **d**. | Output intensity of the device illustrated in **c** at the laser wavelength as a function of the excitation pump power. The cavity mode emission (red dots) shows a kink at the onset of lasing operation, while the background emission (black dots) shows linear dependence. **e**. | Linewidth of the cavity mode emission as a function of the pump power. Inset: Cavity mode emission peaks with increasing pump power shows reduction in linewidth. **f**. | Schematic of a laser device, consisting of a $MoSe_2/WSe_2$ heterostructure on a gravity cavity. **g**. | Photon occupancy (red) and linewidth (blue) of the TE emission from the device shown in **f** as a function of the excitation pump power showing lasing characteristics. **h**. The coherence length of the device shown in **f** as a function of the excitation pump power. Panels **a** and **b** are from Ref. 140, panels **c**-**e** are from Ref. 141, and panels **f**-**h** are from Ref. 142.

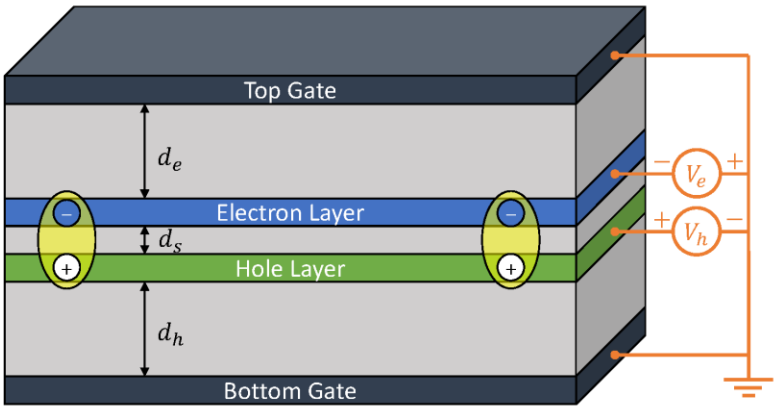

Figure 8 | **Exciton reservoirs in TMD heterostructures.** | In TMD heterostructures, a bias voltage applied between layers acts an exciton reservoir when i) the electron and hole layer contacts have chemical potentials in their respective gaps and ii) the rate of two-particle electron-hole tunneling from the contacts to bound states in the bilayer greatly exceeds the rate of electron or hole tunneling across the tunnel barrier that separates them. These conditions can be established in a TMD heterostructure where the TMD layers are separated by a hexagonal boron nitride tunnel barrier, which can be extremely resistive, even when it is thin enough to allow for large spatially indirect exciton binding energies. In the illustrated case, the top and bottom gates are both grounded, and the electron and hole layers are in contact with reservoirs at voltage $-V_e$ and $+V_h$. When the gate separations d_e and d_h are much larger than the separation d_s between electron and hole layers, large electron and hole densities can easily be generated at overall neutrality. From Ref. 159.

Box 1 | **Topological moiré excitons**

Excitons in monolayer TMDs can be described by the low-energy effective Hamiltonian[25,183–185]:

$$H_0(\boldsymbol{Q}) = \left(\hbar\Omega_0 + \frac{\hbar^2 Q^2}{2M}\right)\tau_0 + JQ\tau_0 + JQ\left(\cos\left(2\phi_Q\right)\tau_x + \sin\left(2\phi_Q\right)\tau_y\right),$$

where $\boldsymbol{Q} = Q\left(\cos\phi_Q\hat{x} + \sin\phi_Q\,\hat{y}\right)$ is the exciton momentum, M is the exciton mass, $\hbar\Omega_0$ is a constant energy, τ_0 and $\tau_{x,y,z}$ are the identity matrix and Pauli matrices in valley pseudospin space, and J represents the strength of exchange interactions. The first term in the Hamiltonian describes the kinetic energy of excitons, the second and third terms describe intravalley and intervalley exchange interactions, respectively. The intervalley exchange interaction acts as an in-plane valley-space pseudo-magnetic field which rotates by 4π when the momentum $\boldsymbol{Q}$ encloses its origin once. This nontrivial winding number can be used to engineer topological exciton bands when combined with the moiré potential. For intralayer moiré excitons in a magnetic field, the low-energy effective Hamiltonian is

$$H = H_0 + \Delta(\boldsymbol{r})\tau_0 + h_z\tau_z,$$

where $\Delta(\boldsymbol{r})$ is the moiré potential and $h_z\tau_z$ is the Zeeman term. The Chern number C of band n is obtained by integrating the Berry curvature,

$$\mathcal{F}_n(\boldsymbol{Q}) = \hat{z}\cdot\nabla_Q \times \left[i\langle\chi_n(\boldsymbol{Q})|\nabla_{\boldsymbol{Q}}|\chi_n(\boldsymbol{Q})\rangle\right],$$

over the mBZ, where $|\chi_n(\boldsymbol{Q})\rangle$ represents the nth eigenstate of H at momentum Q. For the lowest exciton band n = 1, Berry curvature $\mathcal{F}$ is accumulated around γ, κ and κ′ points in the mBZ. The accumulation of $\mathcal{F}$ around γ is induced by the intervalley exchange interaction, and its sign is determined by that of h_z. On the other hand, the accumulation of $\mathcal{F}$ around κ and κ′ is related to the gap opening due to the moiré potential. Integrating $\mathcal{F}$ over the mBZ gives a nonzero Chern

number C over a wide range of parameters (twist angle, potential depth, and phase, h_z). Topological exciton bands are expected to appear routinely in TMD moiré heterostructures.

References:

1. Novoselov, K. S., Mishchenko, A., Carvalho, A. & Castro Neto, A. H. 2D materials and van der Waals heterostructures. *Science* **353**, 1–11 (2016).
2. Wang, L. *et al.* One-dimensional electrical contact to a two-dimensional material. *Science* **342**, 614–617 (2013).
3. Kim, K. *et al.* Van der Waals Heterostructures with High Accuracy Rotational Alignment. *Nano Lett.* **16**, 1989–1995 (2016).
4. Frisenda, R. *et al.* Recent progress in the assembly of nanodevices and van der Waals heterostructures by deterministic placement of 2D materials. *Chem. Soc. Rev.* **47**, 53–68 (2018).
5. Fang, H. *et al.* Strong interlayer coupling in van der Waals heterostructures built from single-layer chalcogenides. *Proc. Natl. Acad. Sci. U. S. A.* **111**, 6198–6202 (2014).
6. Rivera, P. *et al.* Observation of long-lived interlayer excitons in monolayer MoSe 2-WSe 2 heterostructures. *Nat. Commun.* **6**, 4–9 (2015).
7. Yu, H., Liu, G. Bin, Tang, J., Xu, X. & Yao, W. Moiré excitons: From programmable quantum emitter arrays to spin-orbit coupled artificial lattices. *Sci. Adv.* **3**, 1–8 (2017).
8. Jin, C. *et al.* Observation of moiré excitons in WSe2/WS2 heterostructure superlattices. *Nature* **567**, 76–80 (2019).
9. Seyler, K. L. *et al.* Signatures of moiré-trapped valley excitons in MoSe2/WSe2 heterobilayers. *Nature* **567**, 66–70 (2019).
10. Zhang, L. *et al.* Highly valley-polarized singlet and triplet interlayer excitons in van der Waals heterostructure. *Phys. Rev. B* **100**, 1–6 (2019).
11. Wu, F., Lovorn, T. & Macdonald, A. H. Theory of optical absorption by interlayer excitons in transition metal dichalcogenide heterobilayers. *Physical Review B* vol. 97 (2018).
12. Jin, C. *et al.* Identification of spin, valley and moiré quasi-angular momentum of interlayer excitons. *Nat. Phys.* **15**, 1140–1144 (2019).
13. Regan, E. C. *et al.* Mott and generalized Wigner crystal states in WSe2/WS2 moiré superlattices. *Nature* **579**, 359–363 (2020).
14. Tang, Y. *et al.* Simulation of Hubbard model physics in WSe2/WS2 moiré superlattices. *Nature* **579**, 353–358 (2020).
15. Xu, Y. *et al.* Correlated insulating states at fractional fillings of moiré superlattices. *Nature* **587**, 214–218 (2020).
16. Wang, Q. H., Kalantar-Zadeh, K., Kis, A., Coleman, J. N. & Strano, M. S. Electronics and optoelectronics of two-dimensional transition metal dichalcogenides. *Nat. Nano* **7**, 699–712 (2012).
17. Xia, F., Wang, H., Xiao, D., Dubey, M. & Ramasubramaniam, A. Two-dimensional material nanophotonics. *Nat. Photonics* **8**, 899–907 (2014).
18. Mak, K. F. & Shan, J. Photonics and optoelectronics of 2D semiconductor transition metal dichalcogenides. *Nat. Photonics* **10**, 216–226 (2016).
19. Mueller, T. & Malic, E. Exciton physics and device application of two-dimensional transition metal dichalcogenide semiconductors. *npj 2D Mater. Appl.* **2**, 1–12 (2018).
20. Wang, G. *et al.* Colloquium: Excitons in atomically thin transition metal dichalcogenides. *Rev. Mod. Phys.* **90**, 21001 (2018).
21. Splendiani, A. *et al.* Emerging photoluminescence in monolayer MoS2. *Nano Lett.* **10**,

1271–1275 (2010).
22. Mak, K. F., Lee, C., Hone, J., Shan, J. & Heinz, T. F. Atomically thin MoS2: A new direct-gap semiconductor. *Phys. Rev. Lett.* **105**, 2–5 (2010).
23. Xiao, D., Yao, W. & Niu, Q. Valley-contrasting physics in graphene: Magnetic moment and topological transport. *Phys. Rev. Lett.* **99**, 1–4 (2007).
24. Yao, W., Xiao, D. & Niu, Q. Valley-dependent optoelectronics from inversion symmetry breaking. *Phys. Rev. B - Condens. Matter Mater. Phys.* **77**, 1–7 (2008).
25. Wu, F., Qu, F. & Macdonald, A. H. Exciton band structure of monolayer MoS2. *Phys. Rev. B - Condens. Matter Mater. Phys.* **91**, 1–8 (2015).
26. Ramasubramaniam, A. Large excitonic effects in monolayers of molybdenum and tungsten dichalcogenides. *Phys. Rev. B - Condens. Matter Mater. Phys.* **86**, 1–6 (2012).
27. Chernikov, A. *et al.* Exciton binding energy and nonhydrogenic Rydberg series in monolayer WS2. *Phys. Rev. Lett.* **113**, 1–5 (2014).
28. Ye, Z. *et al.* Probing excitonic dark states in single-layer tungsten disulphide. *Nature* **513**, 214–218 (2014).
29. Cao, T. *et al.* Valley-selective circular dichroism of monolayer molybdenum disulphide. *Nat. Commun.* **3**, (2012).
30. Mak, K. F., He, K., Shan, J. & Heinz, T. F. Control of valley polarization in monolayer MoS2 by optical helicity. *Nat. Nanotechnol.* **7**, 494–498 (2012).
31. Zeng, H., Dai, J., Yao, W., Xiao, D. & Cui, X. Valley polarization in MoS 2 monolayers by optical pumping. *Nat. Nanotechnol.* **7**, 490–493 (2012).
32. Sallen, G. *et al.* Robust optical emission polarization in MoS 2 monolayers through selective valley excitation. *Phys. Rev. B - Condens. Matter Mater. Phys.* **86**, 3–6 (2012).
33. Xu, X., Yao, W., Xiao, D. & Heinz, T. F. Spin and pseudospins in layered transition metal dichalcogenides. *Nat. Phys.* **10**, 343–350 (2014).
34. Mak, K. F., Xiao, D. & Shan, J. Light–valley interactions in 2D semiconductors. *Nat. Photonics* **12**, 451–460 (2018).
35. Zhu, Z. Y., Cheng, Y. C. & Schwingenschlögl, U. Giant spin-orbit-induced spin splitting in two-dimensional transition-metal dichalcogenide semiconductors. *Phys. Rev. B - Condens. Matter Mater. Phys.* **84**, 1–5 (2011).
36. Xiao, D., Liu, G. Bin, Feng, W., Xu, X. & Yao, W. Coupled spin and valley physics in monolayers of MoS 2 and other group-VI dichalcogenides. *Phys. Rev. Lett.* **108**, 1–5 (2012).
37. Liu, G. Bin, Xiao, D., Yao, Y., Xu, X. & Yao, W. Electronic structures and theoretical modelling of two-dimensional group-VIB transition metal dichalcogenides. *Chem. Soc. Rev.* **44**, 2643–2663 (2015).
38. Zhao, W. *et al.* Evolution of electronic structure in atomically thin sheets of ws 2 and wse2. *ACS Nano* **7**, 791–797 (2013).
39. Zeng, H. *et al.* Optical signature of symmetry variations and spin-valley coupling in atomically thin tungsten dichalcogenides. *Sci. Rep.* **3**, 2–6 (2013).
40. Echeverry, J. P., Urbaszek, B., Amand, T., Marie, X. & Gerber, I. C. Splitting between bright and dark excitons in transition metal dichalcogenide monolayers. *Phys. Rev. B* **93**, 1–5 (2016).
41. Komider, K., González, J. W. & Fernández-Rossier, J. Large spin splitting in the conduction band of transition metal dichalcogenide monolayers. *Phys. Rev. B - Condens. Matter Mater. Phys.* **88**, 1–7 (2013).

42. Malic, E. *et al.* Dark excitons in transition metal dichalcogenides. *Phys. Rev. Mater.* **2**, 1–7 (2018).
43. Zhang, X. X., You, Y., Zhao, S. Y. F. & Heinz, T. F. Experimental Evidence for Dark Excitons in Monolayer WSe2. *Phys. Rev. Lett.* **115**, 1–6 (2015).
44. Komsa, H. P. & Krasheninnikov, A. V. Electronic structures and optical properties of realistic transition metal dichalcogenide heterostructures from first principles. *Phys. Rev. B - Condens. Matter Mater. Phys.* **88**, 1–7 (2013).
45. Koåmider, K. & Fernández-Rossier, J. Electronic properties of the MoS2-WS2 heterojunction. *Phys. Rev. B - Condens. Matter Mater. Phys.* **87**, 2–5 (2013).
46. Gong, C. *et al.* Band alignment of two-dimensional transition metal dichalcogenides: Application in tunnel field effect transistors. *Appl. Phys. Lett.* **103**, (2013).
47. Zhang, C. *et al.* Systematic study of electronic structure and band alignment of monolayer transition metal dichalcogenides in Van der Waals heterostructures. *2D Mater.* **4**, (2017).
48. Raja, A. *et al.* Coulomb engineering of the bandgap and excitons in two-dimensional materials. *Nat. Commun.* **8**, 1–7 (2017).
49. Waldecker, L. *et al.* Rigid Band Shifts in Two-Dimensional Semiconductors through External Dielectric Screening. *Phys. Rev. Lett.* **123**, 206403 (2019).
50. Rivera, P. *et al.* Valley-polarized exciton dynamics in a 2D semiconductor heterostructure. *Science* **351**, 688–691 (2016).
51. Wu, F. C., Xue, F. & Macdonald, A. H. Theory of two-dimensional spatially indirect equilibrium exciton condensates. *Phys. Rev. B - Condens. Matter Mater. Phys.* **92**, 1–13 (2015).
52. Wang, Z. *et al.* Evidence of high-temperature exciton condensation in two-dimensional atomic double layers. *Nature* **574**, 76–80 (2019).
53. Heo, H. *et al.* Interlayer orientation-dependent light absorption and emission in monolayer semiconductor stacks. *Nat. Commun.* **6**, 1–7 (2015).
54. Nayak, P. K. *et al.* Probing Evolution of Twist-Angle-Dependent Interlayer Excitons in MoSe2/WSe2 van der Waals Heterostructures. *ACS Nano* **11**, 4041–4050 (2017).
55. Yan, W. *et al.* Probing Angle-Dependent Interlayer Coupling in Twisted Bilayer WS2. *J. Phys. Chem. C* **123**, 30684–30688 (2019).
56. Hong, X. *et al.* Ultrafast charge transfer in atomically thin MoS2/WS2 heterostructures. *Nat. Nanotechnol.* **9**, 682–686 (2014).
57. Ceballos, F., Bellus, M. Z., Chiu, H. Y. & Zhao, H. Ultrafast charge separation and indirect exciton formation in a MoS2-MoSe2 van der waals heterostructure. *ACS Nano* **8**, 12717–12724 (2014).
58. Ross, J. S. *et al.* Interlayer Exciton Optoelectronics in a 2D Heterostructure p-n Junction. *Nano Lett.* **17**, 638–643 (2017).
59. Jauregui, L. A. *et al.* Electrical control of interlayer exciton dynamics in atomically thin heterostructures. *Science* **366**, 870–875 (2019).
60. Liu, K. *et al.* Evolution of interlayer coupling in twisted molybdenum disulfide bilayers. *Nat. Commun.* **5**, 1–6 (2014).
61. Van Der Zande, A. M. *et al.* Tailoring the electronic structure in bilayer molybdenum disulfide via interlayer twist. *Nano Lett.* **14**, 3869–3875 (2014).
62. Meckbach, L., Stroucken, T. & Koch, S. W. Influence of the effective layer thickness on the ground-state and excitonic properties of transition-metal dichalcogenide systems. *Phys. Rev. B* **97**, 1–15 (2018).

63. Arora, A. *et al.* Interlayer excitons in a bulk van der Waals semiconductor. *Nat. Commun.* **8**, 1–6 (2017).
64. Horng, J. *et al.* Observation of interlayer excitons in MoSe2 single crystals. *Phys. Rev. B* **97**, 1–5 (2018).
65. Wang, Z., Chiu, Y. H., Honz, K., Mak, K. F. & Shan, J. Electrical Tuning of Interlayer Exciton Gases in WSe2 Bilayers. *Nano Lett.* **18**, 137–143 (2018).
66. Wu, F., Lovorn, T. & Macdonald, A. H. Topological Exciton Bands in Moiré Heterojunctions. *Phys. Rev. Lett.* **118**, 1–6 (2017).
67. Zhang, C. *et al.* Interlayer couplings, Moiré patterns, and 2D electronic superlattices in MoS2/WSe2 hetero-bilayers. *Sci. Adv.* **3**, 1–8 (2017).
68. Wu, F., Lovorn, T., Tutuc, E. & MacDonald, A. H. Hubbard model physics in transition metal dichalcogenide Moiré bands. *arXiv* (2018).
69. Naik, M. H. & Jain, M. Ultraflatbands and Shear Solitons in Moiré Patterns of Twisted Bilayer Transition Metal Dichalcogenides. *Phys. Rev. Lett.* **121**, 266401 (2018).
70. Gillen, R. & Maultzsch, J. Interlayer excitons in MoSe2/WSe2 heterostructures from first principles. *Phys. Rev. B* **97**, 1–7 (2018).
71. Naik, M. H., Maity, I., Maiti, P. K. & Jain, M. Kolmogorov-Crespi Potential for Multilayer Transition-Metal Dichalcogenides: Capturing Structural Transformations in Moiré Superlattices. *J. Phys. Chem. C* **123**, 9770–9778 (2019).
72. Naik, M. H., Kundu, S., Maity, I. & Jain, M. Origin and evolution of ultraflat bands in twisted bilayer transition metal dichalcogenides: Realization of triangular quantum dots. *Phys. Rev. B* **102**, 1–11 (2020).
73. Enaldiev, V. V., Zólyomi, V., Yelgel, C., Magorrian, S. J. & Fal'ko, V. I. Stacking Domains and Dislocation Networks in Marginally Twisted Bilayers of Transition Metal Dichalcogenides. *Phys. Rev. Lett.* **124**, (2020).
74. Weston, A. *et al.* Atomic reconstruction in twisted bilayers of transition metal dichalcogenides. *Nat. Nanotechnol.* **15**, 592–597 (2020).
75. McGilly, L. J. *et al.* Visualization of moiré superlattices. *Nat. Nanotechnol.* **15**, 580–584 (2020).
76. Rosenberger, M. R. *et al.* Twist Angle-Dependent Atomic Reconstruction and Moiré Patterns in Transition Metal Dichalcogenide Heterostructures. *ACS Nano* **14**, 4550–4558 (2020).
77. Zhang, Z. *et al.* Flat bands in twisted bilayer transition metal dichalcogenides. *Nat. Phys.* **16**, 1093–1096 (2020).
78. Waters, D. *et al.* Flat Bands and Mechanical Deformation Effects in the Moiré Superlattice of MoS2-WSe2Heterobilayers. *ACS Nano* **14**, 7564–7573 (2020).
79. Li, H. *et al.* Imaging moiré flat bands in three-dimensional reconstructed WSe2/WS2 superlattices. *Nat. Mater.* (2021) doi:10.1038/s41563-021-00923-6.
80. Tang, Y. *et al.* Tuning layer-hybridized moiré excitons by the quantum-confined Stark effect. *Nat. Nanotechnol.* **2**, (2020).
81. Andersen, T. I. *et al.* Excitons in a reconstructed moiré potential in twisted WSe2/WSe2 homobilayers. *Nat. Mater.* (2021) doi:10.1038/s41563-020-00873-5.
82. Macneill, D. *et al.* Breaking of valley degeneracy by magnetic field in monolayer MoSe2. *Phys. Rev. Lett.* **114**, 1–5 (2015).
83. Srivastava, A. *et al.* Valley Zeeman effect in elementary optical excitations of monolayer WSe 2. *Nat. Phys.* **11**, 141–147 (2015).

84. Aivazian, G. *et al.* Magnetic control of valley pseudospin in monolayer WSe 2. *Nat. Phys.* **11**, 148–152 (2015).
85. Kim, J. *et al.* Ultrafast generation of pseudo-magnetic field for valley excitons in WSe2 monolayers. *Science* **346**, 1205–1208 (2014).
86. Sie, E. J. *et al.* Valley-selective optical Stark effect in monolayer WS2. *Nat. Mater.* **14**, 290–294 (2015).
87. Yu, H., Wang, Y., Tong, Q., Xu, X. & Yao, W. Anomalous Light Cones and Valley Optical Selection Rules of Interlayer Excitons in Twisted Heterobilayers. *Phys. Rev. Lett.* **115**, 1–5 (2015).
88. Lu, X., Li, X. & Yang, L. Modulated interlayer exciton properties in a two-dimensional moiré crystal. *Phys. Rev. B* **100**, 155416 (2019).
89. Geng, W. T., Wang, V., Liu, Y. C., Ohno, T. & Nara, J. Moiré Potential, Lattice Corrugation, and Band Gap Spatial Variation in a Twist-Free MoTe2/MoS2 Heterobilayer. *J. Phys. Chem. Lett.* **11**, 2637–2646 (2020).
90. Joe, A. Y. *et al.* Electrically controlled emission from singlet and triplet exciton species in atomically thin light emitting diodes. *arXiv* 17–21 (2020).
91. Ciarrocchi, A. *et al.* Polarization switching and electrical control of interlayer excitons in two-dimensional van der Waals heterostructures. *Nat. Photonics* **13**, 131–136 (2019).
92. Wang, T. *et al.* Giant Valley-Zeeman Splitting from Spin-Singlet and Spin-Triplet Interlayer Excitons in WSe2/MoSe2 Heterostructure. *Nano Lett.* **20**, 694–700 (2020).
93. Miller, B. *et al.* Long-Lived Direct and Indirect Interlayer Excitons in van der Waals Heterostructures. *Nano Lett.* **17**, 5229–5237 (2017).
94. Hanbicki, A. T. *et al.* Double Indirect Interlayer Exciton in a MoSe2/WSe2 van der Waals Heterostructure. *ACS Nano* **12**, 4719–4726 (2018).
95. Tran, K. *et al.* Evidence for moiré excitons in van der Waals heterostructures. *Nature* **567**, 71–75 (2019).
96. Calman, E. V. *et al.* Indirect Excitons and Trions in MoSe2/WSe2 van der Waals Heterostructures. *Nano Lett.* **20**, 1869–1875 (2020).
97. Bai, Y. *et al.* Excitons in strain-induced one-dimensional moiré potentials at transition metal dichalcogenide heterojunctions. *Nat. Mater.* **19**, 1068–1073 (2020).
98. Wang, J. *et al.* Diffusivity Reveals Three Distinct Phases of Interlayer Excitons in MoSe2/WSe2 Heterobilayers.
99. Förg, M. *et al.* Moiré excitons in MoSe2-WSe2 heterobilayers and heterotrilayers. *arXiv* (2020).
100. Kunstmann, J. *et al.* Momentum-space indirect interlayer excitons in transition-metal dichalcogenide van der Waals heterostructures. *Nat. Phys.* **14**, 801–805 (2018).
101. Li, W., Lu, X., Dubey, S., Devenica, L. & Srivastava, A. Dipolar interactions between localized interlayer excitons in van der Waals heterostructures. *Nat. Mater.* **19**, 624–629 (2020).
102. Baek, H. *et al.* Highly energy-tunable quantum light from moiré-trapped excitons. *Sci. Adv.* **6**, 1–7 (2020).
103. Brotons-Gisbert, M. *et al.* Spin–layer locking of interlayer excitons trapped in moiré potentials. *Nat. Mater.* **19**, 630–636 (2020).
104. He, Y. M. *et al.* Single quantum emitters in monolayer semiconductors. *Nat. Nanotechnol.* **10**, 497–502 (2015).
105. Srivastava, A. *et al.* Optically active quantum dots in monolayer WSe 2. *Nat.*

Nanotechnol. **10**, 491–496 (2015).
106. Koperski, M. *et al.* Single photon emitters in exfoliated WSe2 structures. *Nat. Nanotechnol.* **10**, 503–506 (2015).
107. Chakraborty, C., Kinnischtzke, L., Goodfellow, K. M., Beams, R. & Vamivakas, A. N. Voltage-controlled quantum light from an atomically thin semiconductor. *Nat. Nanotechnol.* **10**, 507–511 (2015).
108. Merkl, P. *et al.* Twist-tailoring Coulomb correlations in van der Waals homobilayers. *Nat. Commun.* **11**, 1–7 (2020).
109. Brem, S. *et al.* Hybridized intervalley moiré excitons and flat bands in twisted WSe2bilayers. *Nanoscale* **12**, 11088–11094 (2020).
110. Scuri, G. *et al.* Electrically Tunable Valley Dynamics in Twisted WSe2/WSe2 Bilayers. *Phys. Rev. Lett.* **124**, 1–8 (2020).
111. Ruiz-Tijerina, D. A. & Fal'Ko, V. I. Interlayer hybridization and moiré superlattice minibands for electrons and excitons in heterobilayers of transition-metal dichalcogenides. *Phys. Rev. B* **99**, 30–32 (2019).
112. Alexeev, E. M. *et al.* Resonantly hybridized excitons in moiré superlattices in van der Waals heterostructures. *Nature* **567**, 81–86 (2019).
113. Zhang, L. *et al.* Twist-angle dependence of moiré excitons in WS2/MoSe2 heterobilayers. *Nat. Commun.* **11**, 1–8 (2020).
114. Sung, J. *et al.* Broken mirror symmetry in excitonic response of reconstructed domains in twisted MoSe2/MoSe2 bilayers. *Nat. Nanotechnol.* **15**, 750–754 (2020).
115. Shimazaki, Y. *et al.* Strongly correlated electrons and hybrid excitons in a moiré heterostructure. *Nature* **580**, 472–477 (2020).
116. Hsu, W. T. *et al.* Tailoring excitonic states of van der Waals bilayers through stacking configuration, band alignment and valley-spin. *Sci. Adv.* **5**, 1–6 (2019).
117. Bistritzer, R. & MacDonald, A. H. Moiré bands in twisted double-layer graphene. *Proc. Natl. Acad. Sci. U. S. A.* **108**, 12233–12237 (2011).
118. Cao, Y. *et al.* Correlated insulator behaviour at half-filling in magic-angle graphene superlattices. *Nature* **556**, 80–84 (2018).
119. Chen, G. *et al.* Evidence of a gate-tunable Mott insulator in a trilayer graphene moiré superlattice. *Nat. Phys.* **15**, 237–241 (2019).
120. Allain, A., Kang, J., Banerjee, K. & Kis, A. Electrical contacts to two-dimensional semiconductors. *Nat. Mater.* **14**, 1195–1205 (2015).
121. Ross, J. S. *et al.* Electrical control of neutral and charged excitons in a monolayer semiconductor. *Nat. Commun.* **4**, 1–6 (2013).
122. Mak, K. F. *et al.* Tightly bound trions in monolayer MoS 2. *Nat. Mater.* **12**, 207–211 (2013).
123. Jin, C. *et al.* Stripe phases in WSe2/WS2 moiré superlattices. *arXiv* (2020).
124. Wang, L. *et al.* Correlated electronic phases in twisted bilayer transition metal dichalcogenides. *Nat. Mater.* **19**, 861–866 (2020).
125. Shimazaki, Y. *et al.* Optical signatures of charge order in a Mott-Wigner state. *arXiv* (2020).
126. Liu, X. *et al.* Strong light-matter coupling in two-dimensional atomic crystals. *Nat. Photonics* **9**, 30–34 (2014).
127. Dufferwiel, S. *et al.* Exciton-polaritons in van der Waals heterostructures embedded in tunable microcavities. *Nat. Commun.* **6**, 1–7 (2015).

128. Basov, D. N., Fogler, M. M. & García De Abajo, F. J. Polaritons in van der Waals materials. *Science* **354**, (2016).
129. Flatten, L. C. *et al.* Room-Temperature exciton-polaritons with two-dimensional WS 2. *Sci. Rep.* **6**, 1–7 (2016).
130. Sidler, M. *et al.* Fermi polaron-polaritons in charge-tunable atomically thin semiconductors. *Nat. Phys.* **13**, 255–261 (2017).
131. Liu, X. *et al.* Control of Coherently Coupled Exciton Polaritons in Monolayer Tungsten Disulphide. *Phys. Rev. Lett.* **119**, 1–6 (2017).
132. Chen, Y. J., Cain, J. D., Stanev, T. K., Dravid, V. P. & Stern, N. P. Valley-polarized exciton-polaritons in a monolayer semiconductor. *Nat. Photonics* **11**, 431–435 (2017).
133. Dufferwiel, S. *et al.* Valley-addressable polaritons in atomically thin semiconductors. *Nat. Photonics* **11**, 497–501 (2017).
134. Zhang, L., Gogna, R., Burg, W., Tutuc, E. & Deng, H. Photonic-crystal exciton-polaritons in monolayer semiconductors. *Nat. Commun.* **9**, 1–8 (2018).
135. Fogler, M. M., Butov, L. V. & Novoselov, K. S. High-temperature superfluidity with indirect excitons in van der Waals heterostructures. *Nat. Commun.* **5**, 1–5 (2014).
136. Gupta, S., Kutana, A. & Yakobson, B. I. Heterobilayers of 2D materials as a platform for excitonic superfluidity. *Nat. Commun.* **11**, 1–7 (2020).
137. Lee, C. H. *et al.* Atomically thin p-n junctions with van der Waals heterointerfaces. *Nat. Nanotechnol.* **9**, 676–681 (2014).
138. Förg, M. *et al.* Cavity-control of interlayer excitons in van der Waals heterostructures. *Nat. Commun.* **10**, 1–6 (2019).
139. Latini, S., Ronca, E., De Giovannini, U., Hübener, H. & Rubio, A. Cavity Control of Excitons in Two-Dimensional Materials. *Nano Lett.* **19**, 3473–3479 (2019).
140. Rivera, P. *et al.* Coupling of photonic crystal cavity and interlayer exciton in heterobilayer of transition metal dichalcogenides. *2D Mater.* **7**, (2020).
141. Liu, Y. *et al.* Room temperature nanocavity laser with interlayer excitons in 2D heterostructures. *Sci. Adv.* **5**, 1–6 (2019).
142. Paik, E. Y. *et al.* Interlayer exciton laser of extended spatial coherence in atomically thin heterostructures. *Nature* **576**, 80–84 (2019).
143. Zhang, L. Van der Waals Heterostructure Polaritons with Moiré-Induced Nonlinearity. *Nature* (2021).
144. Blatt, J. M., Böer, K. W. & Brandt, W. Bose-Einstein condensation of excitons. *Phys. Rev.* **126**, 1691 (1962).
145. Keldysh, L. V & Kozlov, A. N. Collective properties of excitons in semiconductors. *Sov. Phys. JETP* **27**, 521 (1968).
146. Lozovik, Y. E. & Yudson, V. I. A new mechanism for superconductivity: pairing between spatially separated electrons and holes. *Zh. Eksp. i Teor. Fiz* **71**, 738–753 (1976).
147. Fukuzawa, T., Mendez, E. E. & Hong, J. M. Phase transition of an exciton system in GaAs coupled quantum wells. *Phys. Rev. Lett.* **64**, 3066 (1990).
148. Zhu, X., Littlewood, P. B., Hybertsen, M. S. & Rice, T. M. Exciton condensate in semiconductor quantum well structures. *Phys. Rev. Lett.* **74**, 1633 (1995).
149. Alexandrou, A. *et al.* Electric-field effects on exciton lifetimes in symmetric coupled GaAs/Al0.3Ga0.7As double quantum wells. *Phys. Rev. B* **42**, 9225 (1990).
150. Butov, L. V, Zrenner, A., Abstreiter, G., Böhm, G. & Weimann, G. Condensation of indirect excitons in coupled AlAs/GaAs quantum wells. *Phys. Rev. Lett.* **73**, 304 (1994).

151. Butov, L. V, Gossard, A. C. & Chemla, D. S. Macroscopically ordered state in an exciton system. *Nature* **418**, 751–754 (2002).
152. Fisher, D. S. & Hohenberg, P. C. Dilute Bose gas in two dimensions. *Phys. Rev. B* **37**, 4936 (1988).
153. Prokof'ev, N., Ruebenacker, O. & Svistunov, B. Critical point of a weakly interacting two-dimensional Bose gas. *Phys. Rev. Lett.* **87**, 270402 (2001).
154. Filinov, A., Prokof'Ev, N. V. & Bonitz, M. Berezinskii-kosterlitz-thouless transition in two-dimensional dipole systems. *Phys. Rev. Lett.* **105**, 2–5 (2010).
155. Perali, A., Neilson, D. & Hamilton, A. R. High-temperature superfluidity in double-bilayer graphene. *Phys. Rev. Lett.* **110**, 146803 (2013).
156. Su, J.-J. & MacDonald, A. H. Spatially indirect exciton condensate phases in double bilayer graphene. *Phys. Rev. B* **95**, 45416 (2017).
157. Burg, G. W. *et al.* Strongly enhanced tunneling at total charge neutrality in double-bilayer graphene-WSe2 heterostructures. *Phys. Rev. Lett.* **120**, 177702 (2018).
158. Xie, M. & MacDonald, A. H. Electrical reservoirs for bilayer excitons. *Phys. Rev. Lett.* **121**, 67702 (2018).
159. Zeng, Y. & MacDonald, A. H. Electrically controlled two-dimensional electron-hole fluids. *Phys. Rev. B* **102**, 85154 (2020).
160. Ma, L. *et al.* Strongly correlated excitonic insulator in atomic double layers. *arXiv* (2021).
161. Eisenstein, J. P. & MacDonald, A. H. Bose-Einstein condensation of excitons in bilayer electron systems. *Nature* **432**, 691–694 (2004).
162. Spielman, I. B., Eisenstein, J. P., Pfeiffer, L. N. & West, K. W. Resonantly enhanced tunneling in a double layer quantum Hall ferromagnet. *Phys. Rev. Lett.* **84**, 5808 (2000).
163. Kellogg, M., Eisenstein, Jp., Pfeiffer, L. N. & West, K. W. Vanishing Hall resistance at high magnetic field in a double-layer two-dimensional electron system. *Phys. Rev. Lett.* **93**, 36801 (2004).
164. Tutuc, E., Shayegan, M. & Huse, D. A. Counterflow measurements in strongly correlated GaAs hole bilayers: evidence for electron-hole pairing. *Phys. Rev. Lett.* **93**, 36802 (2004).
165. Fisher, M. P. A., Weichman, P. B., Grinstein, G. & Fisher, D. S. Boson localization and the superfluid-insulator transition. *Phys. Rev. B* **40**, 546–570 (1989).
166. Greiner, M. *et al.* Quantum phase transition from a superfluid to a Mott insulator in an ultracold gas of atoms. *Phys. B Condens. Matter* **329**–**333**, 11–12 (2003).
167. Jung, J., Raoux, A., Qiao, Z. & Macdonald, A. H. Ab initio theory of moiré superlattice bands in layered two-dimensional materials. *Phys. Rev. B - Condens. Matter Mater. Phys.* **89**, 1–18 (2014).
168. Togan, E., Lim, H. T., Faelt, S., Wegscheider, W. & Imamoglu, A. Enhanced Interactions between Dipolar Polaritons. *Phys. Rev. Lett.* **121**, 227402 (2018).
169. Tsintzos, S. I. *et al.* Electrical Tuning of Nonlinearities in Exciton-Polariton Condensates. *Phys. Rev. Lett.* **121**, 37401 (2018).
170. Cristofolini, P. *et al.* Coupling quantum tunneling with cavity photons. *Science* **336**, 704–707 (2012).
171. Delteil, A. *et al.* Towards polariton blockade of confined exciton–polaritons. *Nat. Mater.* **18**, 219–222 (2019).
172. Muñoz-Matutano, G. *et al.* Emergence of quantum correlations from interacting fibre-cavity polaritons. *Nat. Mater.* **18**, 213–218 (2019).
173. Emmanuele, R. P. A. *et al.* Highly nonlinear trion-polaritons in a monolayer

semiconductor. *Nat. Commun.* **11**, (2020).
174. Kyriienko, O., Krizhanovskii, D. N. & Shelykh, I. A. Nonlinear Quantum Optics with Trion Polaritons in 2D Monolayers: Conventional and Unconventional Photon Blockade. *Phys. Rev. Lett.* **125**, 197402 (2020).
175. Dreismann, A. *et al.* A sub-femtojoule electrical spin-switch based on optically trapped polariton condensates. *Nat. Mater.* **15**, 1074–1078 (2016).
176. Kavokin, A. & Lagoudakis, P. Exciton-polariton condensates: Exciton-mediated superconductivity. *Nat. Mater.* **15**, 599–600 (2016).
177. Cortese, E. *et al.* Excitons bound by photon exchange. *Nat. Phys.* **17**, 31–35 (2021).
178. Paravicini-Bagliani, G. L. *et al.* Magneto-transport controlled by Landau polariton states. *Nat. Phys.* **15**, 186–190 (2019).
179. Ashida, Y. *et al.* Quantum Electrodynamic Control of Matter: Cavity-Enhanced Ferroelectric Phase Transition. *Phys. Rev. X* **10**, 1–33 (2020).
180. Laussy, F. P., Kavokin, A. V. & Shelykh, I. A. Exciton-polariton mediated superconductivity. *Phys. Rev. Lett.* **104**, 1–4 (2010).
181. Cotleţ, O., Zeytinolu, S., Sigrist, M., Demler, E. & Imamolu, A. Superconductivity and other collective phenomena in a hybrid Bose-Fermi mixture formed by a polariton condensate and an electron system in two dimensions. *Phys. Rev. B* **93**, 1–19 (2016).
182. Qiu, L., Chakraborty, C., Dhara, S. & Vamivakas, A. N. Room-temperature valley coherence in a polaritonic system. *Nat. Commun.* **10**, 1–5 (2019).
183. Yu, H., Liu, G.-B., Gong, P., Xu, X. & Yao, W. Dirac cones and Dirac saddle points of bright excitons in monolayer transition metal dichalcogenides. Nature communications, 5(1)-1–7, 2014. .pdf. *Nat. Commun.* **5**, 1–7 (2014).
184. Yu, T. & Wu, M. W. Valley depolarization due to intervalley and intravalley electron-hole exchange interactions in monolayer MoS2. *Phys. Rev. B - Condens. Matter Mater. Phys.* **89**, 1–7 (2014).
185. Glazov, M. M. *et al.* Exciton fine structure and spin decoherence in monolayers of transition metal dichalcogenides. *Phys. Rev. B - Condens. Matter Mater. Phys.* **89**, (2014).

Acknowledgements: E.Y.P., Y.Z., L.Z., J.Z., A.H.M., H.D., and F.W. acknowledge support from the US Army Research Office under MURI award W911NF-17-1-0312. E.Y.P, L.Z., and H.D. were also supported by the Air Force Office of Scientific Research under award FA2386-18-1-4086 and the National Science Foundation under award DMR 1838412. D. W. was supported by the US Department of Energy, Office of Science, Office of Basic Energy Sciences, Materials Sciences and Engineering Division under contract number DE-AC02-05-CH11231 (van der Waals heterostructures programme, KCWF16). E.C.R. acknowledges support from the Department of Defense through the National Defense Science & Engineering Graduate Fellowship (NDSEG) Program.

Author contributions: All authors contributed to the writing of the manuscript.

Competing Interests: The authors declare no competing interests.